

POLITECNICO DI TORINO

Master's Degree in Energy and Nuclear Engineering



**Politecnico
di Torino**

Master's Degree Thesis

**Evaluating Radionuclide Detection
Technologies: A Study of Stationary TGS
and Dynamic 3D Gamma Imaging
Systems in Radiological Characterisation**

Supervisor

Prof. Raffaella TESTONI

Co-Advisor

Dr. Filippo GAGLIARDI

Candidate

Lorenzo LONGO

Academic Year 2024-2025

Abstract

Radiological characterisation plays a crucial role in nuclear engineering, providing essential tools for the accurate assessment and management of radioactive materials across diverse sectors, including nuclear decommissioning and CBRN (Chemical, Biological, Radiological, and Nuclear) threat mitigation. Innovations are underway to enable specialists to operate safely from a distance.

This thesis conducts a comparative analysis of radionuclide detection and imaging technologies, focusing on two distinct systems. The first is the Tomographic Gamma Scanner (TGS), a stationary device that utilises a High-Purity Germanium (HPGe) detector for 3D analysis of object matrix density and radionuclide activity. The second is a portable gamma-ray imaging spectrometer, equipped with a Cadmium Zinc Telluride (CZT) detector. On its own, this detector performs 2D Gamma Imaging reconstructions, employing both Compton Imaging and Coded Aperture Imaging techniques along with an optical camera. When integrated with the SLAM-based imaging system GammAware, it further provides 3D Gamma Imaging capabilities, significantly enhancing its functional scope.

The primary goal of this research is to assess the imaging and reconstruction capabilities of the stationary TGS setup versus the dynamic, portable system. For this comparison, sources of caesium, americium, and cobalt were placed within a common reference structure to evaluate the quality of the reconstructions. This involves a thorough comparison of outputs from both systems, focusing particularly on the detailed reconstructions provided by the portable system, especially when augmented by the GammAware for 3D point cloud generation of scenes and sources. These reconstructions are carefully analysed, offering a novel comparison of environmental reconstructions achieved through LIDAR, utilised by GammAware, and photogrammetry, which provides a more realistic colour representation of the scene.

The findings from this analysis highlight the significant capabilities and some limitations of the two technologies, suggesting areas for future development to enhance their application in radiological assessments.

Table of Contents

1	Introduction	1
1.1	Context and Motivations	1
1.2	Objectives of the Thesis	2
1.3	Structure of the Document	3
2	Theoretical Foundations	5
2.1	The Interconnection of Energy, Mass, and Radiation	5
2.1.1	Radionuclides and Their Characteristics	5
2.1.2	Fundamental Concepts and Units in Radiation Protection	6
2.2	Gamma Rays: Properties and Characteristics	9
2.2.1	Nature and Energy Range of Gamma Rays	9
2.2.2	Mechanisms of Interaction of Gamma Rays with Matter	10
2.3	Introduction to Radiation Detection	11
2.3.1	Detector Working Principle	12
2.3.2	Detectors Characteristics and Efficiency	14
2.3.3	Energy Spectrum Structure	15
2.3.4	Background	16
2.4	Semiconductor Detectors for High Resolution Radiation Measurement	17
2.4.1	HPGe Detectors	18
2.4.2	CdZnTe Detectors	18
2.4.3	Comparison of HPGe and CZT Detectors	19
3	Gamma Imaging and Tomographic Techniques	23
3.1	Gamma Imaging in Pixelated CZT Detectors: Theory and Practice	23
3.1.1	Compton Imaging	25
3.1.2	Coded-Aperture Imaging	25
3.1.3	Combining Gamma Imaging with Optical Cameras	27
3.2	The GammAware System for 3D Imaging and Spatial Mapping	28
3.3	H3D Visualizer 3D: Software for Analysis and Visualisation	30
3.4	Tomographic Gamma Scanner: Principle of Operation	32
3.4.1	Reconstruction Algorithms	33

3.4.2	Resolution and Artefacts	34
3.4.3	Visualisation and Analysis	34
4	Methodology for 3D Reconstruction and Point Cloud Processing	37
4.1	Wedding Cake: Characteristics and Materials	37
4.2	Point Clouds and Photogrammetry in Radiation Mapping	39
4.3	Editing Point Clouds via CloudCompare Software	44
4.3.1	Introduction to Point Clouds and Data Import	44
4.3.2	Point Cloud Alignment and Data Standardisation	45
4.3.3	Fusion of Point Clouds Using CloudCompare	46
4.3.4	Analysis of Radiation Data Using Scalar Fields	47
4.4	Measurement Preparation and Scanning Procedure	48
5	Analysis and Results	53
5.1	Qualitative Analysis of Radiological Clouds Generated with 3D Mapper	53
5.2	Quantitative Analysis Using CloudCompare	61
5.3	Qualitative Analysis of TGS Reconstructions	66
5.4	Calculation of Source Extensions and Quantitative Error Analysis .	72
5.4.1	Quantitative Error Analysis	74
5.4.2	Reconstructed Positions	75
5.4.3	Source Extensions	76
6	Conclusions and Perspectives	77
	Bibliography	79

Chapter 1

Introduction

1.1 Context and Motivations

Radiological characterisation is a fundamental process in nuclear science and radiation protection, aimed at identifying, quantifying, and spatially mapping radionuclides within a given environment. This procedure plays a crucial role in ensuring safety, regulatory compliance, and effective planning for activities involving radioactive materials. Its applications span a wide range of fields, including nuclear facility decommissioning, environmental monitoring, radioactive waste management, and CBRN (Chemical, Biological, Radiological, and Nuclear) risk assessment.

In the context of nuclear decommissioning in Italy, radiological characterisation serves as a critical tool for the safe dismantling of radioactive installations, the management of nuclear waste, and the environmental remediation of affected sites. Accurate characterisation ensures both worker safety and regulatory compliance, facilitating the efficient planning of decontamination and disposal activities.

However, conducting radiological characterisation in controlled zones requires a combination of specialised methodologies and advanced detection technologies. The complexity of the environment, coupled with strict radiation protection requirements, necessitates the use of highly precise and adaptable measurement systems. In this study, two different radiological characterisation approaches were considered, each leveraging distinct detection principles and data processing techniques to achieve accurate and reliable assessments.

3D Mapper:

A portable and dynamic 3D gamma imaging system based on a Cadmium Zinc Telluride (CZT) semiconductor detector. It is designed for real-time radiological mapping and offers flexibility for on-site measurements due to its compact size and mobility.

Tomographic Gamma Scanner (TGS):

A static and high-precision system based on a High-Purity Germanium (HPGe) semiconductor detector. It is primarily used for high-resolution gamma spectroscopy and tomographic analysis, with a larger and more cumbersome setup compared to the 3D Mapper.

The comparison of these two gamma-ray detection and imaging systems is particularly relevant in the nuclear decommissioning field, where new methodologies are needed to improve the efficiency and reliability of radiological assessments. The insights gained from this study contribute to advancing radiation detection methodologies, particularly in complex and constrained operational scenarios.

1.2 Objectives of the Thesis

The primary objective of this thesis is to evaluate and compare two radiological characterisation technologies—the 3D Mapper system and the TGS—to assess their applicability in nuclear decommissioning.

The research aims to:

- Compare the spatial resolution and accuracy of the 3D Mapper and TGS systems in reconstructing radioactive source distributions.
- Investigate the limitations of both technologies, highlighting their respective advantages and constraints in real-world applications.
- Assess the integration of radiological data with 3D spatial mapping through point cloud analysis, a novel approach that enhances data interpretation and supports decision-making processes.
- Explore the fusion of point clouds with photogrammetry to achieve more accurate and detailed reconstructions.

Although one of the initial goals was the full validation of the 3D Mapper system, technical failures—stemming from a malfunction in part of the device—prevented its complete assessment. Despite these setbacks, the available measurements were retained and analysed, as they provided valuable insights and learning opportunities, consistent with common practices in experimental research.

While the data exhibited several limitations, which will be discussed in detail throughout this work, their inclusion remains relevant for a meaningful comparative study. Using TGS as a benchmark, previously validated through established datasets, allowed for a reliable reference point.

The findings of this study contribute to future developments in radiological characterisation, offering useful insights into optimising measurement strategies and

refining data fusion techniques for improved detection, localisation, and analysis of radiological sources across a variety of applications.

1.3 Structure of the Document

This thesis is organised into six chapters, each addressing a specific aspect of the study:

Chapter 2 provides the theoretical background, covering gamma-ray spectroscopy, radiation-matter interactions, and the principles of radiation detection. It also introduces key concepts in nuclear instrumentation relevant to this work.

Chapter 3 describes the imaging systems, detailing their operating principles, technical specifications, and data acquisition processes.

Chapter 4 focuses on the experimental setup used for measurements and discusses the methodologies applied for data processing and point cloud management. Special attention is given to the use of software for post-processing and visualisation.

Chapter 5 presents the experimental results, comparing the analyses performed using the imaging systems. This chapter includes an evaluation of measurement accuracy, spatial data reconstruction, and the applicability of the findings to radiological characterisation tasks.

Chapter 6 summarises the key findings, outlines the challenges encountered during the study, and discusses future perspectives for improving the methodologies and technologies presented.

Chapter 2

Theoretical Foundations

2.1 The Interconnection of Energy, Mass, and Radiation

Mass and energy are the foundational components of our Universe, deeply interconnected through Einstein's mass-energy equivalence, $E = mc^2$. This equation illustrates that mass and energy are representing two forms of the same underlying reality. This profound relationship highlights the ability of mass and energy to transform into one another, forming the basis for phenomena ranging from nuclear reactions to the dynamics of the cosmos.

One noticeable consequence of this equivalence is radiation, the process by which energy propagates through space. Radiation can travel in the form of waves or particles, transferring energy from a source until it interacts with matter through processes such as absorption, scattering, or transmission. This energy transfer is a key mechanism in fields such as nuclear physics and radiological sciences, governing processes like radioactive decay and nuclear fission [1].

Radiation can be broadly classified into two types: *ionising* and *non-ionising* radiation. Ionising radiation possesses enough energy to eject tightly bound electrons from atoms, creating ions and potentially altering the chemical and structural properties of materials. Examples include X-rays, γ -rays, and certain particle radiations. Non-ionising radiation, such as visible light, radio waves, and microwaves, lacks the energy to ionise atoms but interacts with matter through processes like excitation or heating [2].

2.1.1 Radionuclides and Their Characteristics

Radionuclides are unstable atomic nuclei that undergo radioactive decay, emitting radiation as they transition to a more stable state. This decay process results

in the emission of alpha particles, beta particles, or gamma rays, depending on the nuclear transformation involved. Due to their distinct emission characteristics and detectability, radionuclides play a fundamental role in applications such as radiation detection, nuclear safeguards, medical imaging, and industrial monitoring [2].

The radionuclides of interest for this study include:

- Americium-241,
- Caesium-137,
- Cobalt-60.

These radionuclides are commonly used in test measurements to evaluate the performance of radiation detection instruments.

2.1.2 Fundamental Concepts and Units in Radiation Protection

The traditional unit for measuring radiation energy is the *electronvolt* (eV), defined as the kinetic energy gained by an electron accelerated through a potential difference of 1 volt. Commonly used multiples include kiloelectronvolt (keV) and megaelectronvolt (MeV) [3].

Activity

The activity (A) of a radionuclide represents its rate of decay and is described by the fundamental law of radioactive decay:

$$A = \frac{dN}{dt} = -\lambda N, \quad (2.1)$$

where N is the number of radioactive nuclei and λ is the *decay constant*, specific for each radionuclide. Additionally, daughter products formed during decay may also contribute to the source's activity.

The Becquerel (Bq) is the SI unit of activity, defined as one disintegration per second. The historical unit of activity is the Curie (Ci), originally defined as the activity of one gram of pure ^{226}Ra and set to exactly 3.7×10^{10} Bq.

The specific activity of a radionuclide, which represents the activity per unit mass, is given by:

$$\text{Specific activity} = \frac{\text{Activity}}{\text{Mass}} = \frac{\lambda N}{NM/A_v} = \frac{\lambda A_v}{M}, \quad (2.2)$$

where:

- M = is the atomic mass of the radionuclide,
- $A_v = 6.02 \times 10^{23}$ nuclei/mole (Avogadro's number),
- λ = is the decay constant.

It is important to note that activity measures only the rate of disintegration and does not directly indicate the amount of radiation emitted or its biological effects.

Gamma Ray Exposure

Gamma ray exposure (X) quantifies the ability of gamma rays or X rays to ionise air. It is defined as:

$$X = \frac{dQ}{dm} \quad (2.3)$$

where dQ is the differential charge produced and dm is the differential mass of air in which the ionisation occurs.

The SI unit of exposure is the coulomb per kilogram (C/kg). Exposure depends on:

- Source intensity,
- Geometry of the source and detector,
- Attenuation by materials between the source and the measurement point.

Absorbed Dose

While exposure quantifies ionisation in air, absorbed dose (D) measures the energy deposited per unit mass in any medium [3]. It is defined as:

$$D = \frac{dE}{dm} \quad (2.4)$$

where dE is the energy imparted by radiation and dm is the mass of the medium.

The Gray (Gy) is the SI unit of absorbed dose, where $1 \text{ Gy} = 1 \text{ J/kg}$.

Absorbed dose is used to assess the physical energy deposition in a medium. However, biological effects vary depending on radiation type, leading to the concept of equivalent dose.

Equivalent Dose

When evaluating the biological effects of radiation, equal energy absorption per unit mass does not always produce the same damage. This is because different radiation types interact differently with biological tissues.

The linear energy transfer (LET) describes the rate at which energy is deposited along a particle's path [3]. High-LET radiation (e.g., alpha particles, heavy ions) causes more biological damage than low-LET radiation (e.g., gamma rays, beta particles), even if the total absorbed dose is the same.

To account for these differences, the equivalent dose (H_T) is defined as:

$$H_T = \sum_R w_R D_{T,R} \quad (2.5)$$

where $D_{T,R}$ represents the absorbed dose for a specific tissue (T) and radiation type (R), while w_R is the radiation weighting factor.

The Sievert (Sv) is the SI unit of dose equivalent.

For low-LET radiation (e.g., gamma rays, electrons), w_R is unity (1), meaning that 1 Sv = 1 Gy. However, for high-LET radiation (e.g., alpha particles), w_R can be as high as 20, meaning that even a small absorbed dose leads to significant biological effects [4].

Effective Dose

To assess the overall health risk from radiation exposure, the effective dose (E) is used. It accounts for the fact that different tissues have different radiation sensitivities. It is defined as:

$$E = \sum_T w_T H_T = \sum_T w_T \sum_R w_R D_{T,R} \quad (2.6)$$

where w_T is the tissue T weighting factor [4].

The effective dose is also measured in sieverts (Sv).

Effective Dose Rate and Legal Limits

The legal dose limits are usually expressed in terms of effective dose rates referring to the rate at which radiation is absorbed by tissues over time. It is commonly expressed in sieverts per hour (Sv/h) or, for lower intensities, in millisieverts per year (mSv/y).

Regulatory dose limits are set to ensure occupational and public safety. According to Italian Legislative Decree 101/2020 [5] and ICRP guidelines [4], the annual effective dose rates limits are:

- Occupational exposure: 20 mSv/y.
- Public exposure: 1 mSv/y.

2.2 Gamma Rays: Properties and Characteristics

Ionising radiation is classified into three categories:

- Charged particles (e.g., electrons and protons),
- Photons (e.g., gamma rays and X rays),
- Neutrons.

The focus of this study is electromagnetic radiation, specifically gamma rays, which are emitted during nuclear transitions.

2.2.1 Nature and Energy Range of Gamma Rays

Gamma rays are massless and electrically neutral, they exhibit the wave-particle duality characteristic of quantum mechanics, behaving as photons or waves depending on the detection method. Their energies cover a broad spectrum, typically starting around 10 keV—where they overlap with X-rays—and extending to several tens of MeV, depending on the source. Gamma rays from radioactive decay are commonly observed within the range of a few tens of keV to a few MeV.

Notable examples of gamma-ray emissions from radionuclides relevant to this study include:

- 59.5 keV from ^{241}Am ,
- 661.7 keV from ^{137}Cs ,
- 1.173 MeV and 1.332 MeV from ^{60}Co .

These energy values are characteristic of specific isotopes and serve as important signatures in nuclear spectroscopy.

Gamma rays interact with matter both at the atomic scale, via mechanisms such as the photoelectric effect, Compton scattering, and pair production, and at the nuclear scale, through processes like coherent scattering or nuclear resonance absorption.

2.2.2 Mechanisms of Interaction of Gamma Rays with Matter

Gamma-ray detection relies on its interactions with the detector material. These interactions, which vary depending on the gamma-ray energy, play an important role in determining the detector's effectiveness.

At lower gamma energies, the dominant interaction is the photoelectric effect, illustrated in Figure 2.1, where a gamma ray is fully absorbed by an atomic electron, which is subsequently ejected from the atom [6]. This phenomenon is critical for detecting gamma rays, as the ejected electron can be measured to determine the gamma-ray's energy.

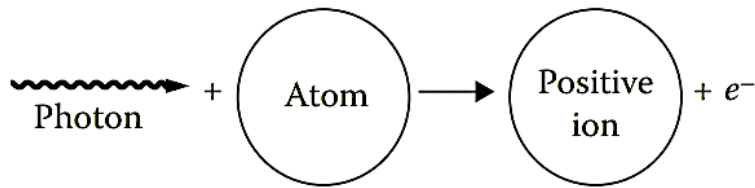


Figure 2.1: The Photoelectric Effect [6]

As gamma energy increases, the primary interaction shifts to the Compton effect, illustrated in Figure 2.2, which is prevalent at intermediate gamma energies. In the Compton effect, a gamma ray collides with an atomic electron, transferring part of its energy to the electron, causing the gamma ray to scatter in a different direction.

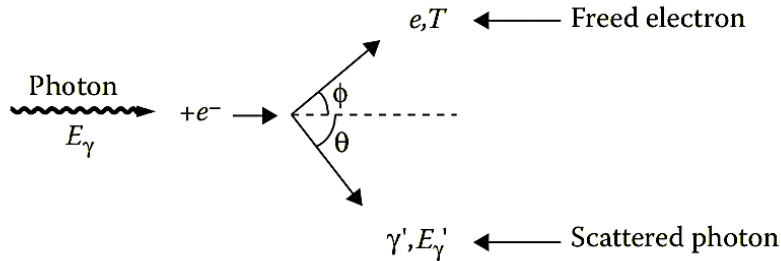


Figure 2.2: The Compton Effect [6]

At higher gamma energies, above 1.022 MeV, pair production can occur. In this process, illustrated in Figure 2.3, a gamma ray is absorbed near the nucleus, resulting in the creation of an electron-positron pair. When the positron annihilates,

it produces two 0.511 MeV gamma rays. While this phenomenon is less common in practical gamma imaging applications, it becomes relevant in scenarios involving high-energy gamma sources.

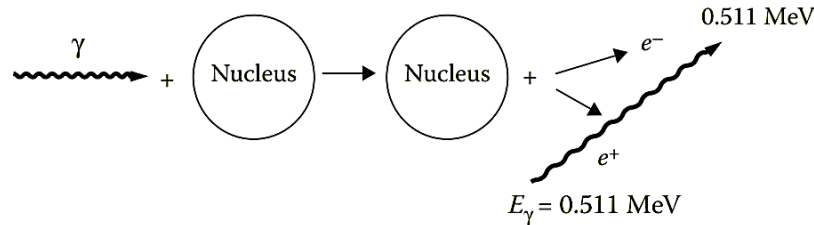


Figure 2.3: Pair Production [6]

As gamma rays travel through materials, they undergo attenuation, a process that gradually reduces their intensity. This attenuation follows an exponential law and depends on both the gamma-ray energy and the properties of the material, such as its type and density [6]. In particular, the penetrating power of gamma rays varies significantly with energy and the density of the medium they traverse [2]. Lower-energy gamma rays are more readily attenuated due to the dominance of the photoelectric effect, while higher-energy gamma rays penetrate deeper before being absorbed or scattered.

These distinct properties make gamma rays invaluable for non-destructive testing (NDT) and various diagnostic applications in nuclear engineering. Their strong penetration capabilities allow for internal characterisation of materials and structures without causing physical damage, making them essential tools in radiography, tomographic imaging, and radiological analysis [7].

2.3 Introduction to Radiation Detection

The main purpose of radiation detectors is to identify, quantify, and analyse radionuclides. Detectors are used in various applications, from basic radiation surveys to advanced nuclear material accountability and forensics. Survey meters, such as Geiger counters, detect surface contamination, while portal monitors identify sources in transit to prevent the unauthorised movement of radioactive materials.

By measuring radiation, detectors provide insights into its properties, including penetration capability, ionisation potential, and the characteristics of the radioactive source, such as decay rate, half-life, and material quantity. For identification, hand-held isotope identifiers and spectroscopy detectors analyse the unique gamma ray or particle emissions specific to each isotope [8].

A radiation detector utilises the mechanisms of radiation interaction with matter to gather information about the radiation itself. These mechanisms are significant when they result in energy deposition within the detector. A material is a good candidate for radiation detection if these energy deposition mechanisms occur with high probability [9].

An effective gamma detector requires a crystal material with a high atomic number (Z), as this increases the probability of gamma-ray interactions, enabling the material to absorb a significant portion of the radiation. This property is particularly important in gamma spectrometers, where the detector crystal must not only detect gamma rays but also measure its energy with precision.

Another critical factor for gamma detectors is their ability to accurately distinguish between different gamma-ray energies. This characteristic, known as *resolution*, determines the detector's capability to clearly separate closely spaced gamma-ray peaks in an energy spectrum. The importance of resolution will be explored in greater detail in the following section.

In advanced applications, radiation detectors not only identify but also quantify radioactive substances, determining the amount of each radioactive source present. This capability is critical not only in nuclear forensics, controlling special nuclear materials like uranium and plutonium, and managing minor actinides like americium and californium, but also in tasks such as source removal, inventory determination, transportation classification, and deposition in national repositories [10].

2.3.1 Detector Working Principle

Radiation detectors are devices that typically produce electrical pulses in response to incoming particles. Pulse production occurs in two primary modes: in *current-type* systems, energy acts as a trigger, producing a constant pulse regardless of energy or particle type (e.g., Geiger-Mueller detectors). These are typically used for high-intensity radiation fields, generating a continuous signal, as in ionisation chambers.

In *pulse-type* systems, the response produced by particle interaction is proportional to the energy deposited in the detector. The signal output is a voltage pulse, as shown in Figure 2.4. These systems, called *counters*, include scintillation counters, gas proportional counters, and semiconductor detectors.

Other devices may produce signals like colour changes (emulsions) or traces visible in photographs (bubble or spark chambers), but these are not discussed here.

An ideal pulse-type detector should satisfy the following requirements [6]:

High Detection Efficiency:

Every particle entering the detector should generate a pulse that exceeds the

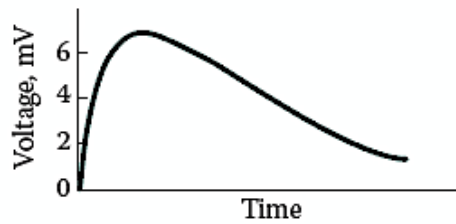


Figure 2.4: Typical voltage pulse in a pulse-type detector [6]

electronic noise level of the subsequent processing unit. This ensures that every particle entering the detector is registered, achieving a *detection efficiency* of 100%, defined as the ratio of detected particles to the total particles entering the detector.

Short Pulse Duration:

The pulse duration should be sufficiently short so that particles entering the detector in rapid succession produce distinct pulses. This minimises the detector's *dead time*, reducing the risk of count losses, especially at high counting rates.

Energy-Dependent Pulse Height:

For accurate energy measurements, the pulse height should have a well-defined relationship with the particle's energy. To achieve this, the detector must be appropriately sized to ensure that particles deposit either all their energy or a known fraction of it within the detector.

Consistent Pulse Height for Identical Energy Deposits:

Particles depositing the same energy in the detector should produce pulses of the same height. This criterion is related to the energy resolution of the detector, which is critical for distinguishing particles of different energies in complex radiation fields.

An example of a good and bad energy resolution can be seen in Figure 2.5.

No detectors can satisfy all these requirements at the same time. For gamma ray detectors, it is not possible to have all the energy of the particle deposited in the counter. Because of statistical effects, there is no detector with ideal energy resolution. Analysts select the detector that satisfies as many of these properties as possible and, depending on the objective of the measurement, apply corrections to the measured data.

The demands on the detector are related to what it is required to know [8]:

- Whether there is a radiation field present.
- The number of nuclear particles that strike a surface per second or some other specified period of time.
- The type of particles present, and, if there are several types, the relative number of each.
- The energy of the individual particles.
- The instant a particle arrives at the detector.

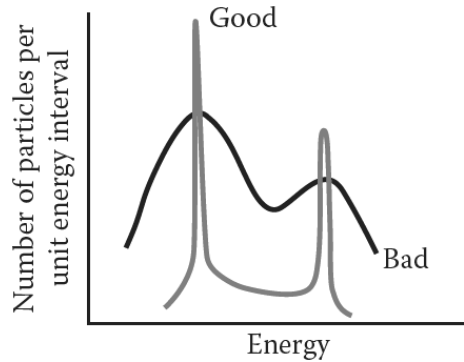


Figure 2.5: Good and bad energy resolution spectra [6]

2.3.2 Detectors Characteristics and Efficiency

Radiation detectors rely on various physical effects to convert radiation into measurable outputs. These sensing methods include electrical, chemical, and light-based approaches. Regardless of the mechanism used, a fundamental property of detectors is their efficiency (ϵ), defined as the fraction of radiation emissions successfully detected [8]:

$$\epsilon = \frac{\text{Radiation emissions counted by detector}}{\text{Radiation emissions from the source}} = \epsilon_g \cdot \epsilon_i \quad (2.7)$$

Here, ϵ_g represents the geometric efficiency, while ϵ_i corresponds to the intrinsic efficiency of the detector. To achieve effective radiation detection, two key factors must be addressed.

First, the *geometry* of the setup must allow sufficient radiation to reach the detector. For example, Figure 2.6 illustrates two common scenarios: radiation surveys using portable instruments (A) and laboratory-based measurements with fixed detectors (B). In survey applications, the detector’s ability to sense radiation depends on the source’s strength and the distance between the source and the detector. Conversely, laboratory setups typically position the sample adjacent to the detector, maximising detection. For a thin-disc sample positioned directly against the detector, approximately half of the emissions are expected to enter the detector material. A configuration in which the detector completely surrounds the sample is referred to as 4π geometry [8].

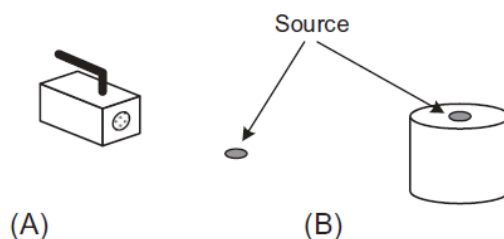


Figure 2.6: Common configurations for radiation measurements: (A) hand-held survey instruments and (B) laboratory detectors for fixed samples [8].

Second, the detector must *effectively* interact with the radiation. If the radiation passes through the detector’s active volume without any interaction, it cannot be detected. Moreover, interactions that do occur must produce signals strong and persistent enough to be measurable.

2.3.3 Energy Spectrum Structure

While some radiation detectors, such as Geiger-Müller counters, are designed solely to detect the presence of radiation without providing energy information, others are specifically engineered to measure the energy deposited by particles [9].

This energy information is derived from the detector’s response, which generates a distribution of voltage pulse heights. These pulse heights correspond to the energy deposited by the radiation within the detector material.

An example of a spectrum can be seen in Figure 2.7, which shows the spectrum of the measurement that will be presented in later chapters. The pulse height distribution acts like a snapshot of the energy deposition processes within the detector and reflects the energy spectrum of the radiation emitted by the measured source.

To obtain this spectrum, a Multichannel Analyser (MCA) is used. The MCA

records and stores the detected pulses, assigning them to specific energy channels and generating an energy spectrum for further analysis.

For radiation with discrete energy levels, the pulse height distribution typically includes distinct features: peaks and continuum regions. Peaks correspond to processes where all the energy of the incoming radiation is absorbed, while the continuum represents cases where only part of the energy is deposited.

The integration of a multichannel analyser (MCA) with this type of device has significantly enhanced the efficiency and accuracy of data collection. The MCA's ability to record the entire energy spectrum simultaneously enables detailed and precise analysis of the detected radiation.

The peaks in the spectrum correspond to total energy absorption processes. By calibrating the detector to establish a relationship between pulse height and energy, the spectrum can provide precise measurements of the radiation's energy.

One key parameter used to quantify a detector's energy resolution is the Full Width at Half Maximum (FWHM) [3]. This metric represents the width of a spectral peak at half of its maximum amplitude and provides a direct measure of the detector's ability to distinguish between gamma rays of similar energies. A smaller FWHM value corresponds to a better energy resolution, enabling clearer separation of nearby gamma peaks. The study of the FWHM is particularly relevant for ^{137}Cs , which emits a gamma ray at 662 keV—a common reference energy in gamma spectroscopy.

As illustrated in Figure 2.7, the CdZnTe detector from H3D Inc. achieves an energy resolution of 0.89% FWHM at 662 keV for ^{137}Cs , highlighting its capability to deliver high-resolution measurements critical for accurate gamma-ray identification.

2.3.4 Background

The detector background can be defined as the number of counts that appear on the counting scale of the system in the absence of a radioactive source [9]. It is crucial to determine and reduce the background of a detector when dealing with samples of low activity. The origin of the detector background is varied [11], comprising several components of either instrumental or fundamental nature.

The laboratory building materials, the air surrounding the detectors, the detector construction materials, the electronic chain, and even the shielding commonly used in a detector system contain radioactive gamma emitting elements. The main contributors are radioactive elements belonging to the natural radioactive series and other primordial radionuclides, such as ^{40}K .

The relative importance of each component depends on the type of detector and the shielding technique used.

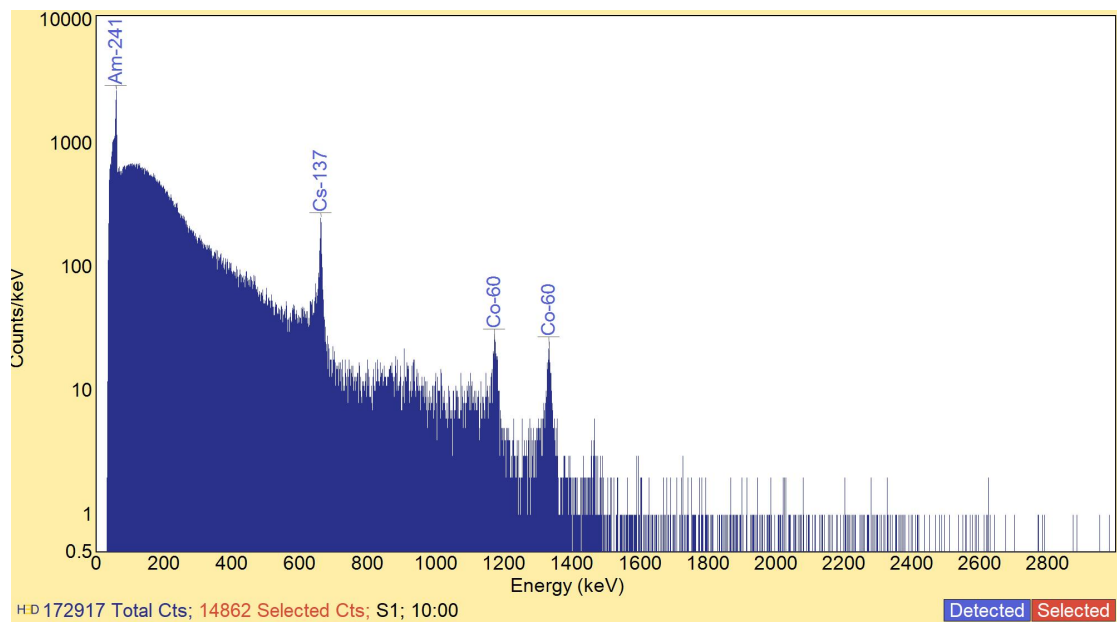


Figure 2.7: Energy spectrum of ^{241}Am , ^{137}Cs and ^{60}Co sources measured with a CdZnTe detector from H3D Inc., demonstrating an energy resolution of 0.89% FWHM at 662 keV for ^{137}Cs . The y -axis shows counts per keV on a logarithmic scale.

2.4 Semiconductor Detectors for High Resolution Radiation Measurement

Radiation detectors can be broadly categorised based on the medium in which radiation interacts. Gas-filled detectors, such as ionisation chambers and proportional counters, rely on ion pair production in gases, requiring higher energy per ionisation event and typically exhibiting lower detection efficiency due to the low density of the medium. In contrast, solid-state detectors, particularly semiconductor detectors, benefit from a much higher atomic density, significantly enhancing the probability of radiation interaction and absorption.

Semiconductor detectors provide superior energy resolution and sensitivity compared to gas-based detectors. When gamma rays interact with a semiconductor crystal, they generate secondary charged particles, which in turn create electron-hole pairs within the material. These charge carriers, separated by an electric field, produce a measurable current pulse that directly reflects the energy of the incident radiation. The lower energy required to produce electron-hole pairs increases accuracy; for example, at 77 K, the energy needed to generate a pair is just 3.86 eV in silicon and 2.97 eV in germanium, compared to 34 eV for an ion pair in gas [2].

Germanium detectors, in particular, take advantage of their well-defined energy gaps and high atomic number to efficiently convert incident gamma rays into measurable charge carriers. This results in a large number of charge pairs per interaction, leading to precise measurements and narrow pulse distributions, making them the preferred choice for high-resolution gamma spectroscopy.

2.4.1 HPGe Detectors

High-Purity Germanium (HPGe) detectors are widely considered the benchmark in gamma spectroscopy due to their significantly better energy resolution compared with other detector technologies [6]. Their crystals are made from ultra-pure germanium, which minimises charge carrier recombination and maximises signal efficiency. These detectors operate at cryogenic temperatures (typically around 77 K) to reduce thermal noise, an essential requirement for achieving their superior performance in high-precision spectroscopy.

This low temperature is often maintained using liquid nitrogen (LN_2) stored in a reservoir, which must be periodically replenished, presenting logistical challenges—particularly in field operations, where portability and maintenance are limiting factors. Alternatively, many modern HPGe detectors employ integrated electro-mechanical cooling systems, thus eliminating the need for liquid nitrogen and reducing some of these logistical issues [12]. However, HPGe crystals require up to 12 hours to reach the operational temperature from room temperature. This process can extend setup and cool down times, ultimately affecting the overall measurement workflow. Recent advancements in HPGe cooling technology aim to mitigate this limitation.

An additional complication arises if an unexpected power loss occurs during operation. In such cases, the detector must first return to ambient temperature before being cooled again, effectively doubling the cooling time. This results in a full thermal cycle lasting up to 24 hours, significantly impacting operational efficiency in field applications.

HPGe detectors are available in different geometries, optimised for specific applications. Coaxial detectors, illustrated in Figure 2.8a, are commonly used in high-resolution gamma spectroscopy, while well-type detectors (Figure 2.8b) are specifically designed for small-volume sources placed inside the well, maximising detection efficiency by increasing the solid angle coverage.

2.4.2 CdZnTe Detectors

Cadmium Zinc Telluride (CZT) detectors have emerged as a compact, room-temperature alternative to HPGe detectors. This semiconductor material is characterised by high resistivity, which helps minimise leakage currents and enhances

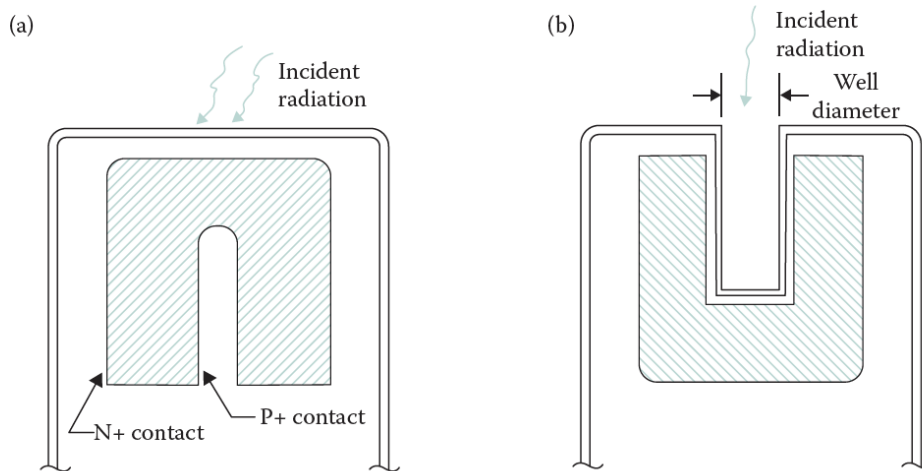


Figure 2.8: Two examples of geometries used for HPGe detectors: (a) coaxial and (b) well type (From Canberra Nuclear, Edition Nine Instruments Catalog.)[6].

signal quality, and a relatively wide bandgap [3], allowing it to operate efficiently at room temperature without significant thermal noise, eliminating the need for any cooling cycle. CZT detectors are characterised by their good energy resolution, as already shown in Figure (2.7), and their relatively high stopping power for gamma rays due to the material’s density and atomic number. However, they are prone to issues such as incomplete charge collection and energy resolution inferior to HPGe detectors. Despite these limitations, advancements in CZT crystal growth and processing techniques continue to enhance their performance and expand their application scope. These detectors are particularly suited for applications requiring portability, such as handheld gamma spectrometers and imaging systems [6].

The CZT detector used for the gamma-ray imaging measurements that are presented in this work is the model H420, from H3D Inc., a very compact and innovative device measuring $24\text{ cm} \times 9.5\text{ cm} \times 18\text{ cm}$ that is shown in Figure 2.9a [13].

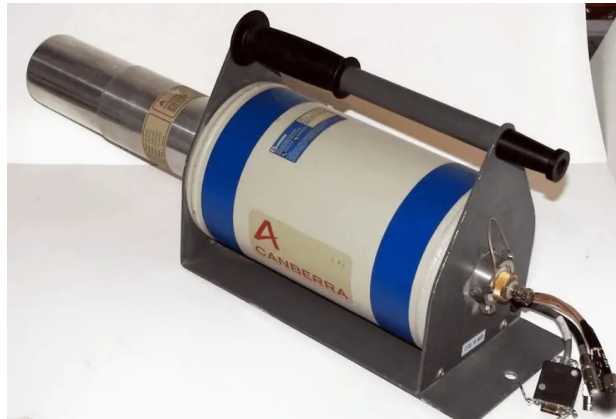
2.4.3 Comparison of HPGe and CZT Detectors

A comparison between CZT and HPGe detectors is shown in Figure 2.9, where the compact design of the CZT detector (Figure 2.9a) is contrasted with the larger HPGe detector (Figure 2.9b), which offers superior energy resolution but requires cryogenic cooling.

High-Purity Germanium (HPGe) and Cadmium Zinc Telluride (CZT) detectors



(a) CZT detector (From H3D Inc., H420 Specifications Sheet)



(b) HPGe detector (From Mirion Technologies (Canberra), Inc.)

Figure 2.9: Comparison of CZT and HPGe detectors. (a) CZT detector with compact design, suitable for portable applications. (b) HPGe detector, known for its superior energy resolution, often used in high-precision measurements.

each offer distinct advantages based on their physical properties and operational characteristics. The choice between these two technologies ultimately depends on the specific requirements of the application. When high energy resolution and detailed spectral analysis are the primary objectives, HPGe remains the preferred option, particularly in controlled laboratory environments where cryogenic cooling constraints are manageable. Conversely, CZT detectors are favoured in applications where portability, rapid deployment, and operational flexibility outweigh the need for ultimate spectral resolution.

In gamma imaging, CZT detectors have become the industry standard due to their small size, lower weight, absence of thermal cycling requirements, and broad applicability. These characteristics make them particularly well-suited for field measurements. Additionally, some CZT-based detectors, including models produced by H3D, can be mounted on drones and terrestrial robots, enabling their use in hazardous or hard-to-reach environments. This capability further enhances their adaptability, making them ideal for remote inspections, large-area surveys, and high-risk radiological assessments.

Newer HPGe-based systems, on the other hand, have demonstrated exceptional performance in imaging isotopes such as ^{235}U and ^{239}Pu , where precise resolution of closely spaced spectral peaks is critical, CZT detectors face some challenges [14].

The industry, anyway, has largely shifted toward CZT-based imaging solutions. This transition is driven not only by the practical advantages of CZT technology

but also by advancements in gamma imaging algorithms. In particular, the algorithms implemented in the H3D’s system—which will be introduced in the next chapter—have significantly enhanced the performance of CZT-based systems in real-world radiological characterisation.

Chapter 3

Gamma Imaging and Tomographic Techniques

This chapter explores the advanced gamma-ray imaging technologies employed in this research. The first system, the state-of-the-art 3D Mapper, combines a CZT detector (Section 3.1) with the GammAware system (Section 3.2). Its proprietary software (Section 3.3) enables the visualisation and interpretation of collected data, offering valuable insights into the spatial distribution of radiation.

The second system, the Tomographic Gamma Scanner (TGS) (Section 3.4), also utilises dedicated proprietary software (Section 3.4.3) for data processing and analysis.

Both instruments, owned and operated by Nucleco, have been fundamental to the data collection and analysis conducted in this work. Their ability to identify hotspots—localised regions with elevated radiation levels—plays a key role in assessing contamination, verifying shielding effectiveness, and optimising safety measures.

3.1 Gamma Imaging in Pixelated CZT Detectors: Theory and Practice

Pixelated CZT detectors are designed to simultaneously measure the energy and the interaction position of incident gamma rays by analysing the electrical signals generated as charge carriers move through the detector material. This process enables precise three-dimensional (3D) localisation of gamma-ray interactions within the detector volume.

These detectors utilise a segmented anode structure, where the anode is divided into an array of square pixels, typically surrounded by a grid electrode for optimised

signal collection [15]. The cathode, in contrast, is a simple planar electrode. Figure 3.1 illustrates an example of a pixelated CZT detector with dimensions of $2\text{ cm} \times 2\text{ cm} \times 1.5\text{ cm}$. The anode features a $11\text{ p} \times 11\text{ p}$ pixel array, with each pixel having a pitch of 1.72 mm, providing high spatial resolution for interaction localisation.

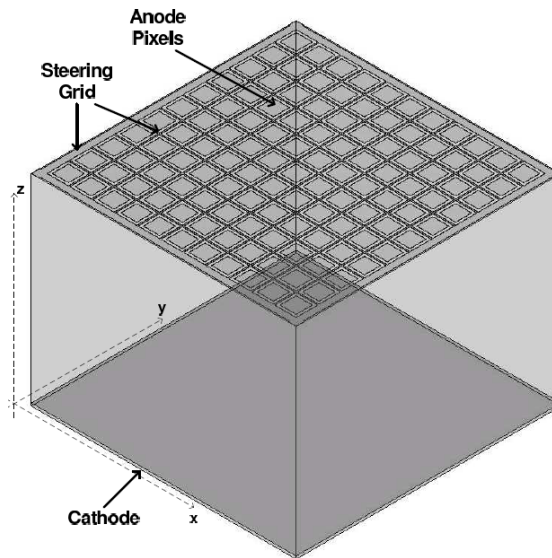


Figure 3.1: Schematic of a CZT detector with pixelated anode and planar cathode. The grid electrode surrounding the pixels aids in charge collection [15].

The method for determining the 3D position of a gamma-ray interaction relies on the following principles:

Depth of Interaction (DOI):

The cathode signal amplitude is proportional to both the DOI and the energy deposited, whereas the signal amplitude on the collecting anode pixel is proportional only to the energy deposited. By calculating the ratio of the cathode signal amplitude to the collecting-anode signal amplitude, as described by He et al. [16], the DOI can be derived.

2D Interaction Position:

The position of the collecting pixel on the anode provides the lateral (x, y) coordinates of the interaction.

3D Reconstruction:

Combining the DOI with the 2D position of the collecting pixel enables the calculation of the 3D interaction position within the detector volume.

This method assumes that only one interaction occurs in the detector volume during the *signal integration time*. For cases with multiple interactions from a single incident gamma ray, later advancements introduced the measurement of electron drift time to resolve multiple DOI positions [17].

Gamma imaging detectors typically capture gamma-ray interaction data within the detector volume; however, this data does not inherently represent an image. As a result, the collected data must be processed to generate a meaningful visual representation [15].

3.1.1 Compton Imaging

Compton imaging is a method that utilises the principles of Compton scattering to locate radiological sources [18]. When incident gamma rays interact within the CZT detector, undergoing Compton scattering followed by photoelectric absorption, the Compton scattering formula can be applied. By combining this formula with the 3D positional and energy data of the detected gamma ray, the scattering angle between the incident and scattered gamma ray is calculated. This angle defines a *ring* of possible source locations, as in Figure 3.2a.

As more gamma ray events are detected, these rings begin to overlap, ultimately converging at the source’s direction, as shown in Figure 3.2b.

This technique, when applied to CZT detectors, is most effective for gamma rays with energies above approximately 250 keV. At these energies, gamma rays are more likely to interact through Compton scattering, which is essential for imaging applications. Conversely, gamma rays with energies below 250 keV predominantly interact through photoelectric absorption, limiting the effectiveness of Compton-based techniques. For such lower-energy gamma ray, alternative imaging methods tailored to their interaction properties must be employed.

3.1.2 Coded-Aperture Imaging

Coded-aperture imaging (CAI) is a technique that evolved from earlier pinhole imaging methods, historically used in medical applications. While pinhole imaging employs a single small aperture to form an image, CAI uses a mask, usually made of tungsten, with a specific pattern of holes, enhancing the detection efficiency and resolution. This approach is particularly suited for gamma rays that interact predominantly via photoelectric absorption within the CZT crystal [18].

The mask allows gamma rays to pass through its patterned holes and interact with the detector. Each detected interaction corresponds to a specific direction, as defined by the geometry of the mask and detector. By recording multiple gamma-ray events, overlapping patterns emerge, which can be used to reconstruct the source’s location, as illustrated in Figure 3.3.

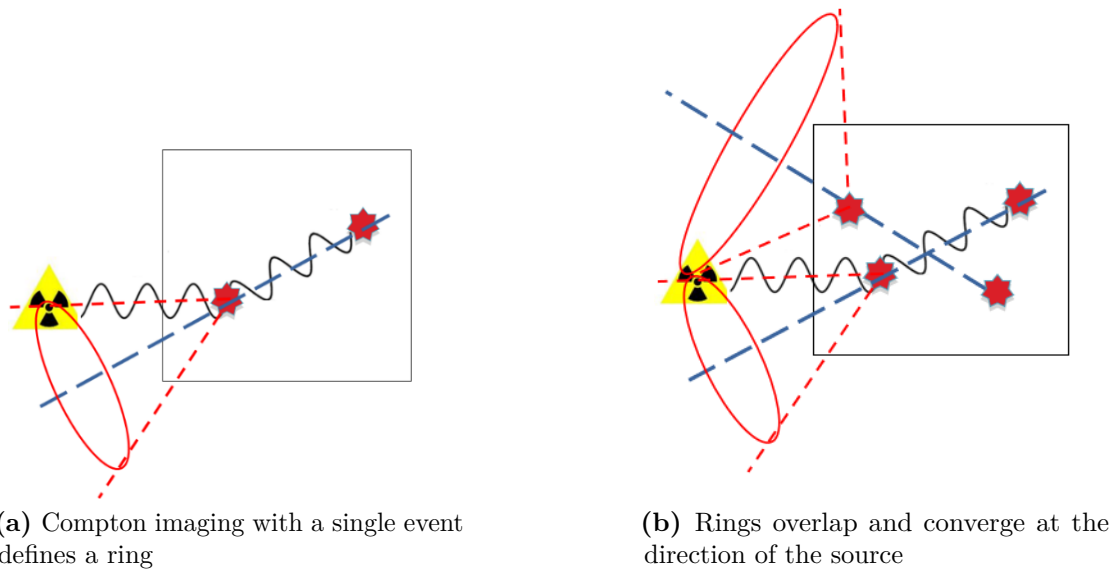


Figure 3.2: Compton imaging technique [18]. (a) A single gamma-ray interaction defines a conical surface of potential source locations, which appears as a ring in 3D space. (b) Multiple Compton events generate overlapping rings, progressively converging to localise the radiological source.

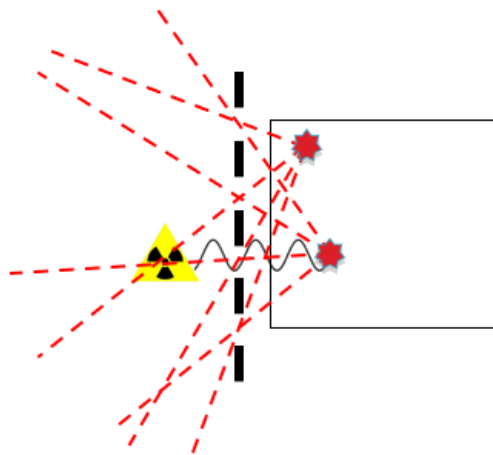


Figure 3.3: Coded aperture imaging technique [18]. A patterned mask modulates incoming gamma rays, producing a shadow pattern on the detector. The recorded signal is then mathematically decoded to reconstruct the spatial distribution of the source.

H3D technology employs CAI for gamma rays with energies up to about 1 MeV. However, as the gamma-ray energy increases, the tungsten mask becomes less effective as a shielding material, reducing the signal-to-noise ratio and requiring a higher statistical sample to achieve accurate imaging. Another limitation of CAI is its restricted field of view, which is limited to the area defined by the mask's geometry, unlike Compton imaging, which offers an omnidirectional field of view.

3.1.3 Combining Gamma Imaging with Optical Cameras

By integrating both Compton and coded-aperture imaging with an optical camera, H3D technology enables radiation to be visualised as illustrated in Figure 3.4 for CAI and in Figure 3.6 for Compton imaging. When the 3D position-sensitive CZT detector is aligned with the optical camera, the radiation maps produced by either imaging technique can be superimposed on optical images. This overlay visually identifies the precise location of radiation sources within the optical field, making it possible to visualise the radiation in the context of the environment [18].



Figure 3.4: Example of CAI reconstruction of a ^{241}Am source in a waste container using the GammAware system.

3.2 The GammAware System for 3D Imaging and Spatial Mapping

The GammAware system, developed by H3D, Inc., combines radiological measurements with spatial mapping capabilities through Simultaneous Localisation and Mapping (SLAM) technology [19]. The system includes a portable frame mounted on a detector, such as the H420 shown in Figure 2.9a. The system integrates a LIDAR device from Ouster and a tracking camera from Intel, ensuring precise alignment between radiation measurements and the physical scene. Data are processed using software based on the Robotic Operating System (ROS) and mapped in real-time using the Cartographer engine [20].

The system provides 3D visualisation of radiation hotspots within a mapped environment. Data are displayed through a web-based interface, which can be accessed simultaneously from multiple devices. The device itself acts as a Wi-Fi hotspot, creating a local network that users can connect to. Once connected, they can access the interface via the device's local IP address. After measurements, post-processing refines the recorded data to generate detailed 3D point clouds that localise radioactive sources with greater precision.

When the GammAware system is integrated with a detector such as the H420, the combined setup is referred to as the 3D Mapper. This system utilises two distinct reconstruction methods to process the acquired data: a real-time approach, which provides immediate visual feedback during data collection, and a post-processing approach, which refines the data after acquisition for improved accuracy and detail.

In real-time mode, the system exclusively uses a simple back-projection (SBP) algorithm to overlay radiation data on a growing 3D grid [12]. As the operator moves, the grid dynamically expands to incorporate newly measured areas, allowing for immediate visualisation of radiation distribution. However, this method offers lower precision and may introduce biases in source localisation due to its simplified processing.

In post-processing mode, the system offers two reconstruction algorithms: Simple Back Projection (SBP) and Maximum Likelihood Expectation Maximisation (MLEM) [18]. SBP is a direct reconstruction method that does not rely on iterative refinement, making it computationally efficient and relatively stable, even with low-statistics data. However, this robustness comes at the cost of reduced spatial resolution and potential image artefacts.

Conversely, MLEM is an iterative technique that gradually improves the reconstruction by maximising the likelihood function under a Poisson distribution model. This approach can achieve higher resolution and better localisation of sources, but it is more sensitive to noise and statistical uncertainties. In cases where data statistics are too low, MLEM may introduce artefacts or fail to converge to a

reliable solution.

Post-processing refines the raw data acquired in real-time, correcting systematic biases and enhancing the final output. However, the application of MLEM in post-processing can sometimes lead to a slight underestimation of the apparent source size due to the smoothing effects inherent in the iterative process. The choice between SBP and MLEM depends on the trade-off between robustness and accuracy, with SBP being preferable in highly challenging conditions and MLEM offering superior performance when sufficient statistics are available.

The output from 3D Mapper consists of raw data that must be processed using dedicated software, Visualizer 3D, which allows for further adjustments and optimisation based on task requirements. Real-time imaging is ideal for quick scans and hotspot identification, while post-processing delivers reliable and detailed scene analysis, making the system versatile for complex environments.



Figure 3.5: 3D Mapper assembled. The GammAware frame is mounted on H3D’s H420 detector [21].

3.3 H3D Visualizer 3D: Software for Analysis and Visualisation

Visualizer 3D is a post-processing tool with a graphical user interface designed for browsing and managing measured data, analysing energy spectra, visualising source distributions for each measurement, and updating the embedded software and settings of H3D detectors [22].

The software operates in two different modes: 2D mode, which is used for analysing stationary measurements and generating images on a spherical surface for Compton imaging and on a Cartesian plane for coded-aperture imaging, and 3D mode, which extends these capabilities to reconstruct and display three-dimensional surfaces and volumes. These modes are accessible through separate tabs within the interface.

The methodologies for post processing are presented in detail:

Reconstruction Resolution:

The system offers two resolution modes for image reconstruction:

SD (Standard Definition):

Uses a back-projection algorithm for reconstruction, providing reliable but slightly blurred results.

HD (High Definition):

Based on the Maximum Likelihood Expectation Maximisation (MLEM) algorithm, this iterative reconstruction technique produces higher-resolution images. However, it requires a statistically robust dataset, as limited data can introduce noise due to the method's sensitivity to measurement statistics.

3D Reconstruction Targets:

Two spatial reconstruction strategies are available:

Full:

Divides the 3D space into cubic voxels along the x, y, and z axes. This method covers the region surrounding the detector path with an additional 1 m buffer in all directions, ensuring comprehensive spatial coverage.

Surfaces:

Limits reconstruction to specific points within a pre-selected point cloud, defined at the start of the imaging process. Unlike full voxelisation, this approach prevents sources from appearing as if they are floating in mid-air, focusing solely on the defined surfaces.

Reconstruction Types:

Two techniques are applied depending on the gamma-ray energy:

Compton:

Designed for gamma rays with energies at or above 250 keV, this method applies Compton imaging, leveraging the scattering interactions of gamma rays.

Coded Aperture:

More effective for gamma rays with energies below 250 keV, this technique uses coded-aperture imaging, which takes advantage of absorption-dominated interactions in this energy range [23].

Figure 3.6 shows an example of a 2D-HD reconstruction, where a ^{60}Co source was identified at the bottom of the drum. The image was reconstructed with the Visualizer 3D after selecting the correct isotope for analysis and automatically superimposed onto the optical image of the scene for better comprehension of the study area.



Figure 3.6: Example of 2D-HD Compton imaging reconstruction using the GammAware system. The ^{60}Co source is located at the bottom of the drum, with the reconstructed gamma image overlaid on the optical image of the scene for enhanced spatial context.

3.4 Tomographic Gamma Scanner: Principle of Operation

The Tomographic Gamma Scanner (TGS) is an advanced segmented gamma spectrometry system designed for the non-destructive assay (NDA) of radioactive waste. It combines high-resolution gamma spectroscopy with tomographic imaging to quantify the radiological content of a drum and reconstruct a 3D image of both the matrix and the contamination distributed within it. This method achieves high accuracy in radionuclide quantification by accounting for non-uniform material distributions and heterogeneous nuclide distributions [24].

The TGS system employs a rotating platform to collect gamma spectra from multiple angles around the object under investigation. Using a High-Purity Germanium (HPGe) detector, the system records gamma-ray intensities and energies emitted by the radioactive sources within the container. As the drum rotates, data are gathered at predefined intervals to create a comprehensive dataset for tomographic reconstruction. This technology has been adopted by Nucleco S.p.A., which installed the system inside a transportable container for on-site operations (see Figure 3.7).



Figure 3.7: The TGS system owned by Nucleco consists of an HPGe detector, a lifting platform for the drum, a roller conveyor for drum transport, and a rotating platform.

The imaging process is divided into two complementary components: transmission imaging and emission imaging. Transmission imaging provides an attenuation map that represents the distribution of the matrix material (i.e., composition and

density), while emission imaging reconstructs the spatial distribution of gamma-emitting radionuclides within the object. The combination of these two datasets allows for accurate corrections of material-specific attenuation losses, enhancing the reliability and accuracy of the final results.

Transmission imaging involves using a certified source to create an attenuation map of the drum's contents [25]. This map reflects the material composition and density by measuring the attenuation of gamma rays as they traverse the object. The attenuation maps are crucial for correcting emission images and ensuring accurate quantification of radionuclides in heterogeneous materials.

Emission imaging reconstructs the spatial distribution of radioactive sources using the data corrected from transmission imaging. The emission data are processed using algorithms like MLEM or ART, which refine the spatial distribution of radionuclides by compensating for the attenuation within the matrix. This method prioritises quantification accuracy over spatial resolution but still provides a valuable visual representation of radioactive source locations.

3.4.1 Reconstruction Algorithms

The TGS employs several advanced algorithms for image reconstruction, each tailored to specific imaging requirements:

Maximum Likelihood Expectation Maximisation (MLEM):

An iterative reconstruction algorithm widely used in emission imaging. It estimates the most likely spatial distribution of radioactive sources by iteratively refining the solution, assuming a Poisson-distributed detection process. By leveraging statistical modelling, MLEM progressively enhances image resolution and accuracy. However, while it effectively reconstructs sources even in challenging conditions, its performance is highly dependent on the available statistical data. In cases of extremely low count rates, the algorithm may introduce artefacts or fail to converge to a reliable solution [26].

Algebraic Reconstruction Technique (ART):

An additive, iterative algorithm used for both transmission and emission imaging. It effectively manages dense materials and heterogeneous matrices by progressively adjusting voxel values to match the measured data. ART is flexible, allowing for constraints such as fixing specific voxel values [26].

Non-Negative Least Squares (NNLS):

This algorithm ensures non-negative voxel values during reconstruction, preventing non-physical results. It is often used as a preliminary step before applying more sophisticated algorithms like MLEM [27].

Ray Tracing Methods:

These methods calculate attenuation matrices for both transmission and emission data, taking into account geometrical factors, such as collimator shape and voxel dimensions [26].

3.4.2 Resolution and Artefacts

The spatial resolution of TGS imaging depends on the voxel size used during reconstruction. For a typical 220-litre drum, voxel dimensions are approximately $5.5 \text{ cm} \times 5.5 \text{ cm} \times 5.5 \text{ cm}$, balancing industrial throughput with the precision needed for accurate radionuclide quantification. Artefacts may arise due to limited resolution, challenging geometries, or insufficient statistical data, particularly in heterogeneous materials, necessitating careful interpretation of the results.

3.4.3 Visualisation and Analysis

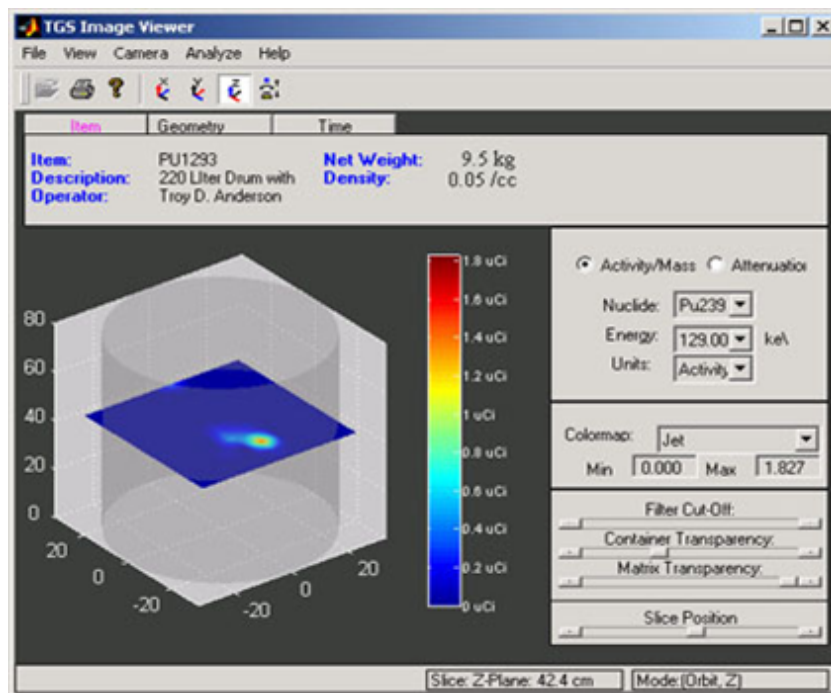


Figure 3.8: TGS Viewer: the software allows for visual examination of ^{239}Pu hotspots and detailed data analysis.

The TGS Viewer, integrated into the NDA 2000 software suite, plays a pivotal role in the interpretation of tomographic gamma scanning data [25]. By offering features

such as animated rotations, sectional views, and surface plots, it enables a detailed visualisation of radiological distributions within complex geometries. These tools facilitate the accurate identification of hotspots and support consistency checks during measurements. Given its extensive use throughout this study, the TGS Viewer has proven to be an indispensable tool for both qualitative and quantitative analysis of radiological data, enhancing the overall reliability of the characterisation process.

Chapter 4

Methodology for 3D Reconstruction and Point Cloud Processing

The experimental activities described in this chapter focus on the reconstruction of radioactive sources placed inside a multi-layered object. Further details about this setup are provided in Section (4.1).

The 3D Mapper system offers a 3D representation of the studied scene along with the corresponding radiological data, generating point clouds that map the radioactive sources contained within the environment. In contrast, the TGS is a static system that produces 3D reconstructions limited to the objects placed on its scanning platform. Techniques for editing and enhancing the point clouds, including the integration of colour through photogrammetry, will be discussed in Section (4.2), providing an alternative to the grey-scale output typically produced by the 3D Mapper system.

4.1 Wedding Cake: Characteristics and Materials

The comparison between the two detectors and related technologies requires a common reference object, known as the Wedding Cake (WC). This name derives from its resemblance to traditional tiered cakes, as the structure is composed of multiple stacked materials forming a layered arrangement.

The first layer consists of stacked wooden disks, resulting in a total height of 25 cm and a diameter of 56.6 cm, with a density of 0.45 g/cm^3 [28].

Above the wooden disks are three paraffin blocks, all shaped as rectangular parallelepipeds. The first and last blocks feature square bases with dimensions

of $30\text{ cm} \times 30\text{ cm} \times 10\text{ cm}$ and a density of 0.83 g/cm^3 [29]. The middle block, however, consists of three adjacent segments with rectangular bases, each measuring $30\text{ cm} \times 10\text{ cm} \times 10\text{ cm}$.

On top of the structure are two cylindrical containers known as Marinelli beakers, which feature a central cavity at the bottom. Each Marinelli beaker has a diameter of 15 cm and a height of 13 cm. These containers are specifically designed for spectroscopic activities involving solid, liquid, or even gaseous sources. The density of the polypropylene, that constitutes the Marinelli is 0.9 g/cm^3 [30].



Figure 4.1: Transparent cylindrical Marinelli beaker for spectroscopy, typically used in radiochemical laboratories [31].

These materials were chosen for their availability and ease of machining, allowing for the precise fabrication of housings for the sources. Both the wooden disks and paraffin slabs were machined, with holes drilled to accommodate the radioactive materials.

The sources used in the setup include:

- A certified ^{241}Am source positioned inside a hole drilled into the wooden disks, with a depth of 10 cm.
- A certified ^{60}Co source placed securely between two stacked Marinelli beakers to ensure stable positioning.
- A certified ^{137}Cs source inserted into a centrally located cavity with a depth of 2 cm within the paraffin slabs.

The entire WC is mounted on a mobile base equipped with a forklift hook, allowing for easy transportation within the area. When using the TGS, the WC is lifted and positioned directly in front of the detector as required for measurement. Conversely, when employing the CZT system, the WC is placed on wooden pallets

on a pavement, a slightly raised area free from vehicle traffic, enabling the operator to move around the scene and capture the complete setup. This configuration is illustrated in Figures 4.2 and 4.3, which provide a detailed representation of the experimental arrangement. The sources used in these measurements were handled exclusively by qualified Nucleco personnel in compliance with the current Italian radiation protection regulations.



Figure 4.2: Illustration of the wedding cake structure.

4.2 Point Clouds and Photogrammetry in Radiation Mapping

Point clouds represent three-dimensional environments through collections of numerous points defined by spatial coordinates, often supplemented with attributes such as colour or intensity. In radiation mapping, they serve as a powerful tool to visualise radiological data within the context of the physical environment.

The GammAware system produces point clouds by integrating spatial data from its LIDAR and camera sensors with radiological measurements. These post-processed point clouds provide detailed environmental maps enriched with radiation

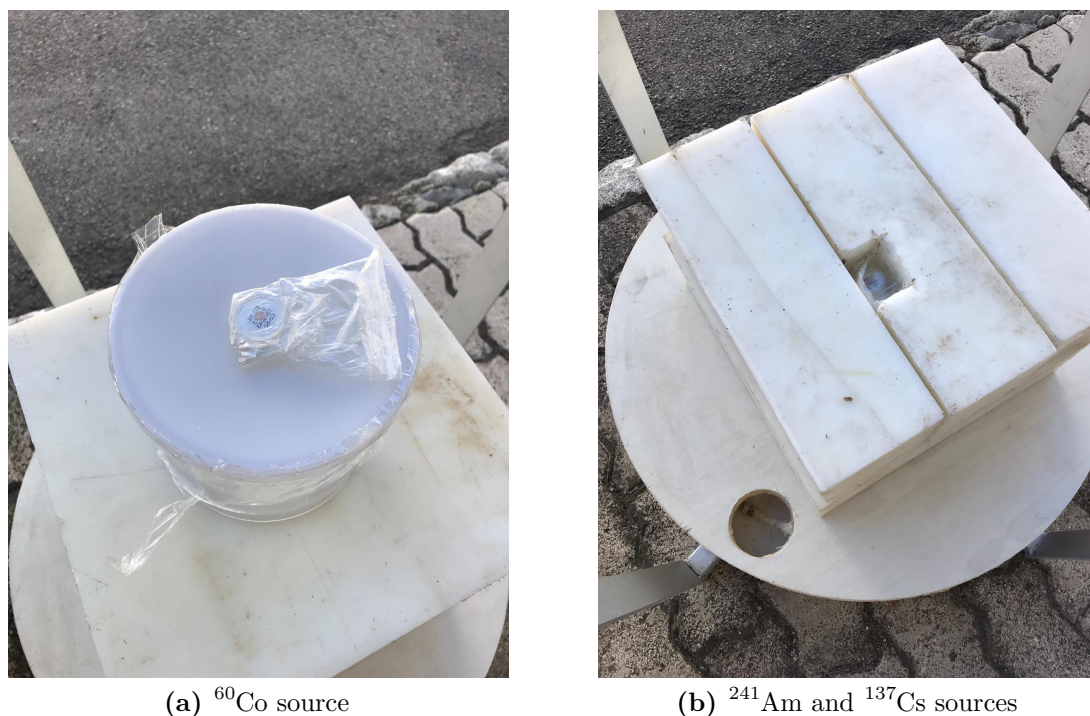


Figure 4.3: Configuration of radioactive sources for the experiment: (a) ^{60}Co positioned between two Marinelli beakers, (b) ^{241}Am embedded within wooden disks and ^{137}Cs placed within a paraffin slab.

intensity information, highlighting areas of interest. However, one major limitation of the GammAware system is the lack of optical RGB (red, green, blue) information in the generated point clouds. This issue, common in devices equipped only with LIDAR technology, makes it more difficult to interpret large datasets, which can contain millions of points. Without colour, it is harder to distinguish object boundaries and their actual dimensions, as shown in Figure 4.4.

Adding RGB data significantly improves the usability of point clouds by allowing users to inspect objects more clearly. Although the GammAware system includes optical cameras that could theoretically solve this problem, hardware and software constraints prevent the acquisition of the many images needed for photogrammetry reconstruction.

To solve this problem, a cost-effective solution was implemented using a smartphone, the Samsung Galaxy S20 Plus, equipped with a 12-megapixel main camera sensor [32]. By using the *Polycam* application, overlapping photos and videos were captured and processed to create textured 3D meshes with colour information [33]. This workflow replicated the operator's movements with the 3D Mapper system,



Figure 4.4: 3D point cloud generated by the GammAware device using LIDAR technology. The image has been extracted from H3D Visualizer 3D and has not been edited, except for the removal of part of the surrounding point cloud, including the floor, to improve clarity in visualising the WC and its components. The Marinelli beaker, highlighted with a red circle, appears poorly reconstructed due to the limitations of LIDAR in capturing transparent or low-reflectivity materials.

ensuring consistency in the reconstruction process. The photos were uploaded to the Polycam cloud for processing, generating a 3D model with better visual clarity. As shown in Figure 4.5, this method produced higher-quality textures, especially along object edges, compared to raw LIDAR data.

Photogrammetry software, such as Polycam, follows a structured pipeline to reconstruct 3D models from a series of overlapping images. The process begins with feature extraction, where unique points such as edges, corners, and textures are identified in multiple photographs and matched across images. Using Structure from Motion (SfM), these 2D points are then used to estimate their 3D positions, forming an initial sparse point cloud [34]. This cloud is subsequently refined into a dense point cloud, containing a much higher number of points to more accurately capture object geometry.

Once the dense point cloud is created, the software generates a polygon mesh by connecting these points into a network of triangular faces, forming a continuous surface representation of the object. This step is performed using triangulation algorithms such as Poisson Surface Reconstruction or other interpolation techniques. Finally, the software applies texturing, where colour information from the original

images is mapped onto the mesh, enhancing its realism and usability.

While meshes are highly effective for visualisation, they lack some of the volumetric and spatial detail preserved in point clouds. Point clouds retain precise positional information for each point, making them more suitable for measurement and analytical applications, such as radiation mapping.

The in-app tools available in Polycam allowed the validation of reconstructed models by comparing the dimensions of objects with their real-world counterparts. Any discrepancies could be corrected by applying a scaling factor to the entire scene. The software also supports exporting files as either polygon meshes or point clouds, ensuring compatibility with various industry-standard formats and workflows.

Another issue addressed using photogrammetry was the reconstruction of the Marinelli beaker. Due to the transparency of its materials and the water it contains, LIDAR systems had difficulty capturing the beaker accurately, as shown in Figure 4.4. To solve this issue, the beaker was wrapped with A4 paper and adhesive tape, as shown in Figure 4.5b. This simple solution allowed for an accurate reconstruction while having a negligible impact on gamma-ray attenuation due to the thinness and low atomic number of the materials used [35].

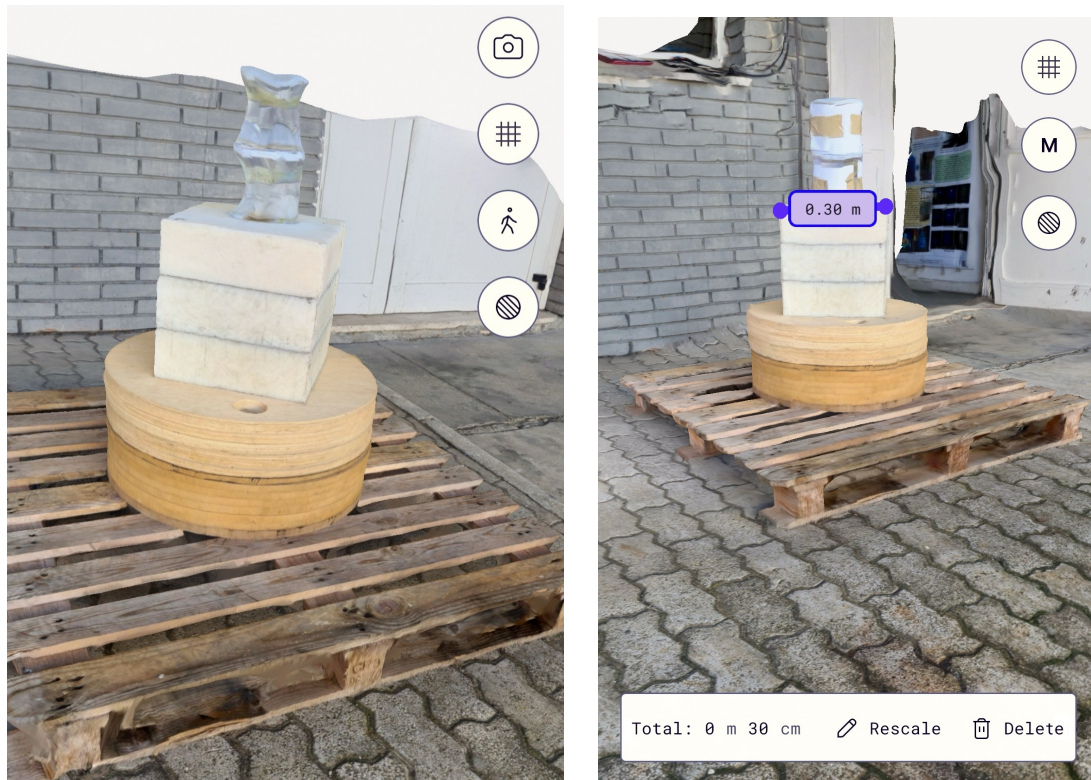


Figure 4.5: Screenshots from the Polycam photogrammetry software [33], captured using a smartphone. (a) Reconstruction of the Marinelli beaker in its uncovered state, showing the original transparency. (b) Reconstruction of the Marinelli beaker covered in paper, performed to enhance the software’s ability to manage transparency. Both images are part of the 3D scene reconstruction.

4.3 Editing Point Clouds via CloudCompare Software

This section introduces the use of CloudCompare software for editing and processing point clouds, aiming to enhance the quality and usability of the 3D data collected. The objective is to provide a comprehensive guide on how to manage and optimise point clouds for accurate radiation mapping and analysis.

4.3.1 Introduction to Point Clouds and Data Import

CloudCompare, an open-source tool for 3D point cloud and mesh visualisation and processing, offers solutions to many challenges associated with point cloud data [36]. It provides a range of features to enhance the accuracy and usability of point clouds, including:

Noise Reduction:

Filtering tools designed to improve the quality of point clouds, particularly when they are derived from a software-generated mesh rather than raw measurement data.

Alignment:

Functions for combining multiple datasets into a single, coherent 3D representation. One tool allows users to manually align two point clouds by selecting at least four equivalent point pairs to establish a reference frame.

Mesh Generation:

Converts point clouds into polygonal meshes to enhance comparison accuracy. When generating a point cloud from a mesh results in poor-quality output, it can be more effective to compare two meshes directly, integrate them, and only then merge the point cloud.

Scalar Fields:

Visualises additional data, such as point intensity or elevation, directly on the point cloud. This feature is extensively used in this study for enhanced analysis and visualisation.

Geometric Functions:

User-friendly tools for operations such as selecting specific points, tracing segments, and calculating surface areas, enabling precise analysis and editing of the 3D data.

CloudCompare supports both *structured* and *unstructured* point clouds, depending on how the data is acquired [37]. Structured point clouds are typically generated

by static scanning systems, such as terrestrial laser scanners, which capture data in a controlled and systematic manner [38]. Due to their organised nature, these datasets are generally easier to process and require fewer computational resources for rendering and alignment.

Conversely, unstructured point clouds, like those produced by GammAware, come from systems in motion and lack a predefined structure. This results in variable point densities, making manipulation and rendering more computationally demanding. Additionally, unstructured point clouds often contain overlapping data and non-uniform sampling, requiring further processing steps such as filtering, resampling, and alignment to enhance accuracy.

In this study, point clouds were imported into CloudCompare from datasets generated using the H3D Visualizer 3D software. The scene point cloud was stored separately from the radiological data point clouds, which were exported as individual .ply files, one for each measured source. These files were generated after the reconstruction performed in H3D Visualizer 3D, following the settings defined in Section (3.3).

4.3.2 Point Cloud Alignment and Data Standardisation

Accurate alignment is crucial for integrating radiological and spatial data. All point clouds generated by the 3D Mapper system are inherently aligned with each other within the same measurement session, ensuring consistent spatial correspondence. However, when integrating data from different sessions or external sources, additional alignment may be necessary. CloudCompare offers several alignment methods, including Iterative Closest Point (ICP), which is widely used for refining point cloud registration. The ICP algorithm keeps one point cloud, the reference (or target), fixed while iteratively transforming the other, the source, to best match it [39]. The transformation, consisting of translation and rotation, is adjusted in successive iterations to minimise an error metric, typically the sum of squared differences between the coordinates of the matched pairs.

While ICP requires an initial estimate of the transformation, it can achieve highly accurate alignment in structured and feature-rich environments. In this study, an example of such an environment is the WC, which was frequently used as a reference for aligning and rescaling the analysed point clouds. The reference cloud, generated by the GammAware system, served as the baseline to which other datasets were adjusted.

Before alignment, data standardisation is essential to ensure consistent and reliable processing. In this context, CloudCompare’s Statistical Outlier Removal (SOR) filter was applied to improve point cloud quality by eliminating sparse noise and erroneous measurements. This method statistically analyses each point’s neighbourhood, removing those whose distances deviate significantly from the

expected distribution [40]. By reducing outliers, the SOR filter enhances the accuracy of subsequent alignment operations, preventing incorrect correspondences and improving overall point cloud integrity, as shown in Figure 4.6.

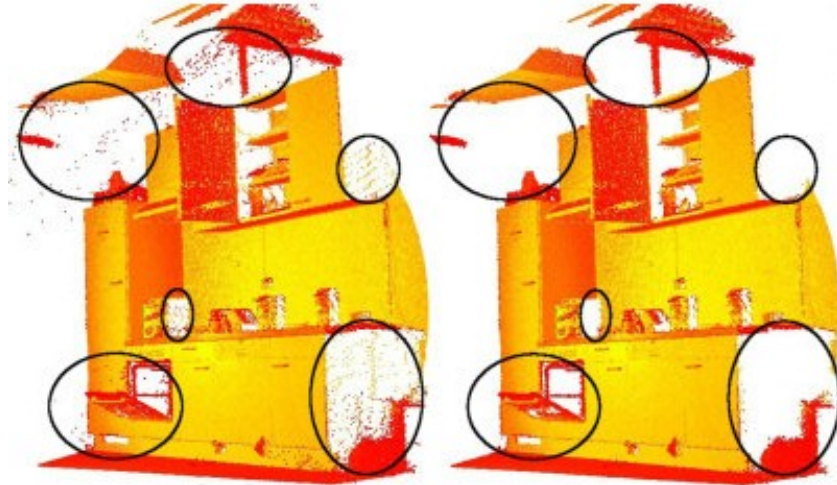


Figure 4.6: Application of the Statistical Outlier Removal (SOR) filter to enhance scene quality. The original dataset is shown on the left, while the filtered dataset is on the right [40].

Additionally, CloudCompare provides a feature-based alignment method, which automatically detects and matches distinctive features within datasets [41]. However, this approach was not utilised in this study, as it relies on well-defined structural elements that may not always be present in the acquired point clouds. Nonetheless, it could be implemented in different contexts that, while not necessarily identical, contain easily distinguishable features against the background. This is particularly relevant for large-scale mapping of decommissioning sites or industrial facilities, where elements such as piping, structural supports, machinery bases, or small storage tanks can serve as reliable reference points for automatic alignment.

4.3.3 Fusion of Point Clouds Using CloudCompare

Merging multiple point clouds is essential for integrating radiological and spatial information. In this study, CloudCompare was used to superimpose the radiological data onto the 3D scene captured by the 3D Mapper system. A key advantage of this approach is that both the scene point cloud and the radiological data point

cloud share the same coordinate system, as they originate from the same acquisition device. This ensures intrinsic alignment between the two datasets, eliminating the need for additional registration steps.

Although H3D Visualizer 3D is also capable of overlaying the reconstructed radiological point cloud onto the scene point cloud, its visualisation tools are highly limited. The software primarily serves as a viewing platform with minimal editing capabilities, making CloudCompare a more suitable choice for further data processing and analysis.

By merging these datasets, the study aims to evaluate the spatial accuracy of radiological data representation within the reconstructed scene. The comparison focuses on assessing whether the detected radiation sources align correctly with the expected physical locations, ensuring that the system provides a reliable depiction of radiation distribution.

To facilitate the visualisation of radiation data, colour maps or scalar fields were applied to highlight radioactive source locations and intensity distributions. This information supports various applications, such as source localisation, contamination assessment, and remediation planning.

4.3.4 Analysis of Radiation Data Using Scalar Fields

Mapping radiation intensity as a scalar field within a 3D environment provides an intuitive way to visualise hotspots, or regions of elevated radiation levels. A scalar field assigns a numerical value to each point in space, allowing radiation intensity to be represented through colour gradients, filtered for improved clarity, or processed with mathematical operations to enhance data interpretation [36].

In this study, radiation intensity values used in the scalar field representation are directly obtained from the 3D Mapper system, as described in Section (3.2). This ensures a high-resolution and spatially accurate mapping of the radiological environment.

Integrating radiation measurements with 3D point clouds requires precise spatial alignment between the detector and the scanned environment. Proper calibration of the 3D Mapper system ensures that radiation intensity values correspond accurately to their physical locations. Any misalignment can introduce errors in data interpretation, emphasising the need for rigorous calibration and validation processes.

4.4 Measurement Preparation and Scanning Procedure

The measurement session consisted of six scans, designed to comprehensively map the environment and collect radiological data for analysis. The setup is illustrated in Figure 4.7, showing an optical view of the scene, while a top-down representation is provided in Figure 4.8.

Following the activation and calibration of the instrument, the first dynamic scan was performed. This initial 10-minute scan served a dual purpose: it mapped the surrounding environment to generate a spatial reference and simultaneously acquired radiological data for further analysis. During this phase, both the LIDAR system and the detector operated simultaneously. A colour-coded heat map was generated based on the measured dose rate distribution, with the scale adjusted to a peak value of 870 nSv/h, as shown in Figure 4.9. The colours range from deep blue, representing background radiation levels, to intense red for the highest recorded dose rates. Intermediate dose levels are visualised with a gradient of green and yellow, providing a clear representation of radiation intensity variations across the scanned area.

After completing the first dynamic scan, the system was positioned on Luggage No. 1 for the first stationary scan. These stationary scans, each lasting 10 minutes, were crucial for improving statistical reliability by allowing the detector to accumulate a higher number of counts from a fixed position. Additionally, the LIDAR system was deactivated to avoid redundant spatial points in the 3D reconstruction.

To transition between stationary scans, shorter dynamic scans of 5 minutes each were performed. The second dynamic scan enabled the system to move from Luggage No. 1 to Luggage No. 2 while updating its position in the scene to ensure coherent data integration. The heat map generated during this scan was rescaled to a new peak dose rate of 520 nSv/h, as depicted in Figure 4.10.

The second stationary scan was then conducted on Luggage No. 2, following the same procedure as the first to ensure consistency in data collection. The third dynamic scan was performed next, allowing the system to transition from Luggage No. 2 to Luggage No. 3, with the heat map scaled to a peak dose rate of 400 nSv/h, as illustrated in Figure 4.11.

Finally, the third stationary scan was carried out on Luggage No. 3, concluding the measurement session and ensuring that all areas of interest were thoroughly analysed.

Software Anomalies in Z-Coordinate Readings During data analysis, discrepancies in the Z-coordinate were identified, particularly at the transitions between scans. A software-related issue caused erroneous vertical shifts in the

recorded position of the detector. This problem was traced to the inertial measurement unit (IMU) within the GammAware system, which exhibited inconsistencies in tracking height changes.

At the end of the first dynamic scan, a vertical drop of 18 cm was observed, as highlighted in Figure 4.12. The Z-coordinate initially recorded at -0.65 m unexpectedly dropped to -0.83 m, likely due to the IMU software. A similar anomaly was detected at the conclusion of the last dynamic scan, where the Z-coordinate, initially at -0.74 m, decreased to -0.83 m, resulting in a 9 cm drop, as illustrated in Figure 4.13. Notably, each time a new dynamic scan commenced, the recorded Z-coordinate returned to a more realistic value, suggesting a software-related offset correction.

These anomalies were taken into account during data processing to prevent misinterpretation of detector positioning and ensure accurate reconstruction of the radiological distribution.



Figure 4.7: Optical image captured by the H420 detector showing the measurement scene. The luggage pieces, the Wedding Cake, and the sources box left on the window ledge are indicated with arrows and labels.

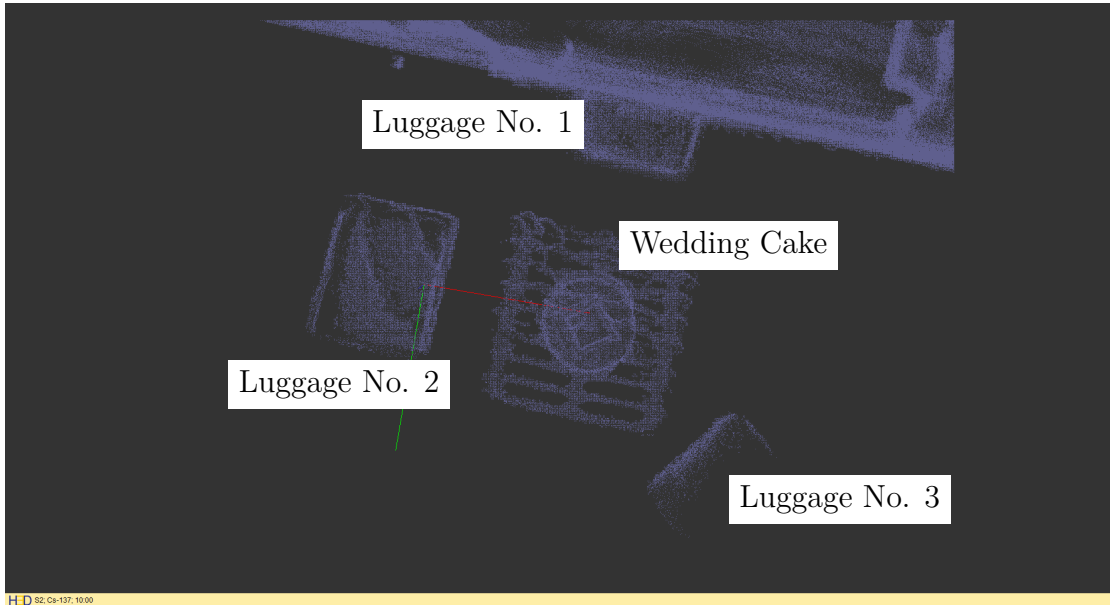


Figure 4.8: Top view of the measurement scene from Visualizer 3D. The WC is centrally positioned, encircled by three pieces of luggage that denote the locations of the stationary scans.

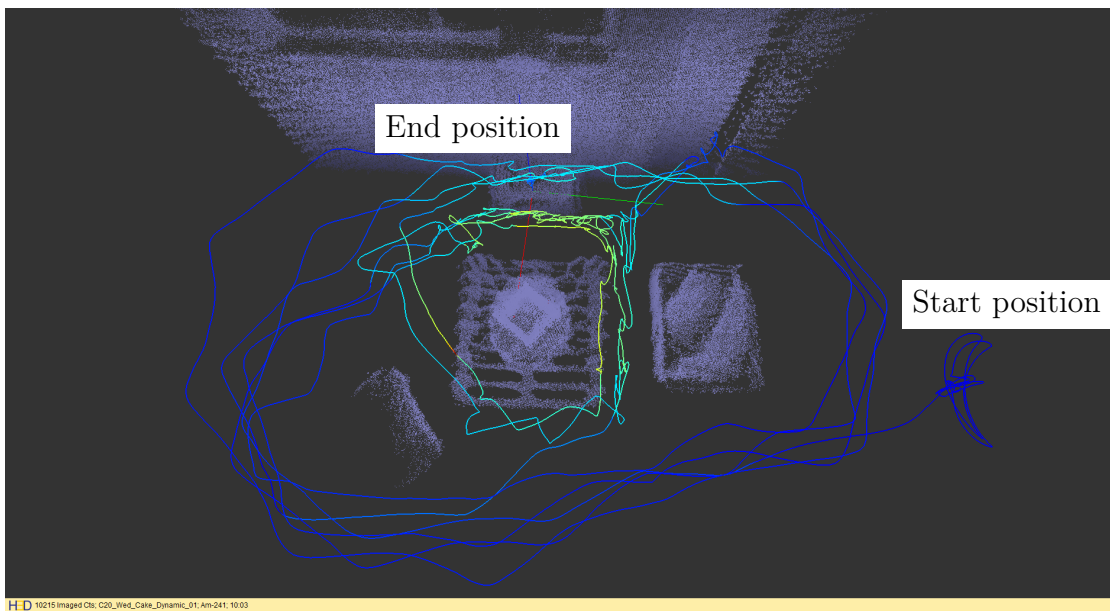


Figure 4.9: Path followed by the operator during the first scan. The starting and ending points, the latter near Luggage No. 1, are labelled. The colour-coded heat map is scaled to a peak dose rate of 870 nSv/h.

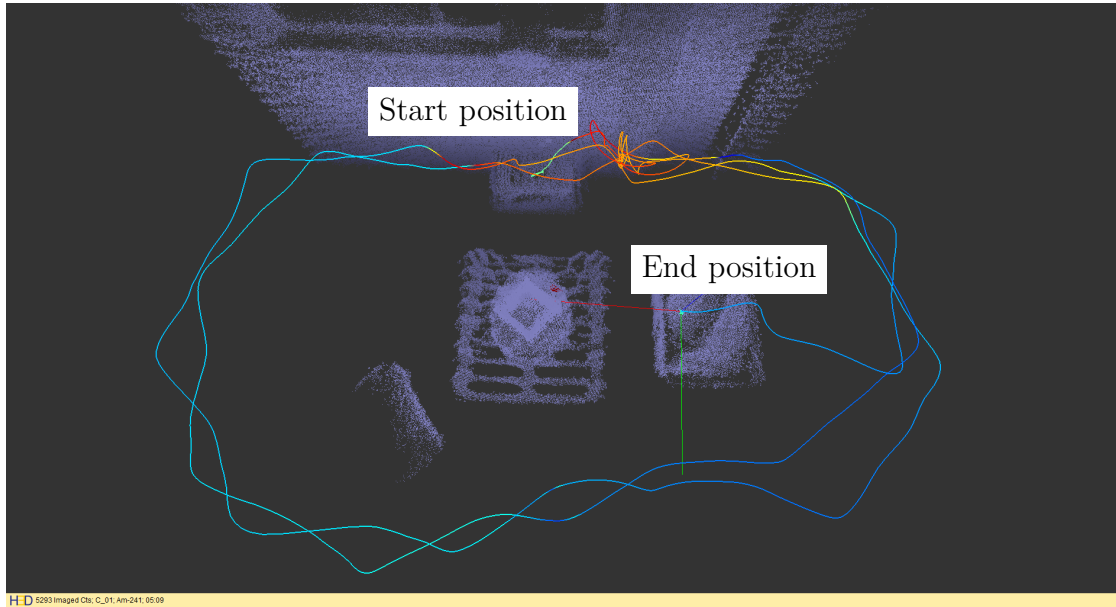


Figure 4.10: Path followed by the operator during the second scan. The starting and ending points, the latter near Luggage No. 2, are labelled. The colour-coded heat map is scaled to a peak dose rate of 520 nSv/h.

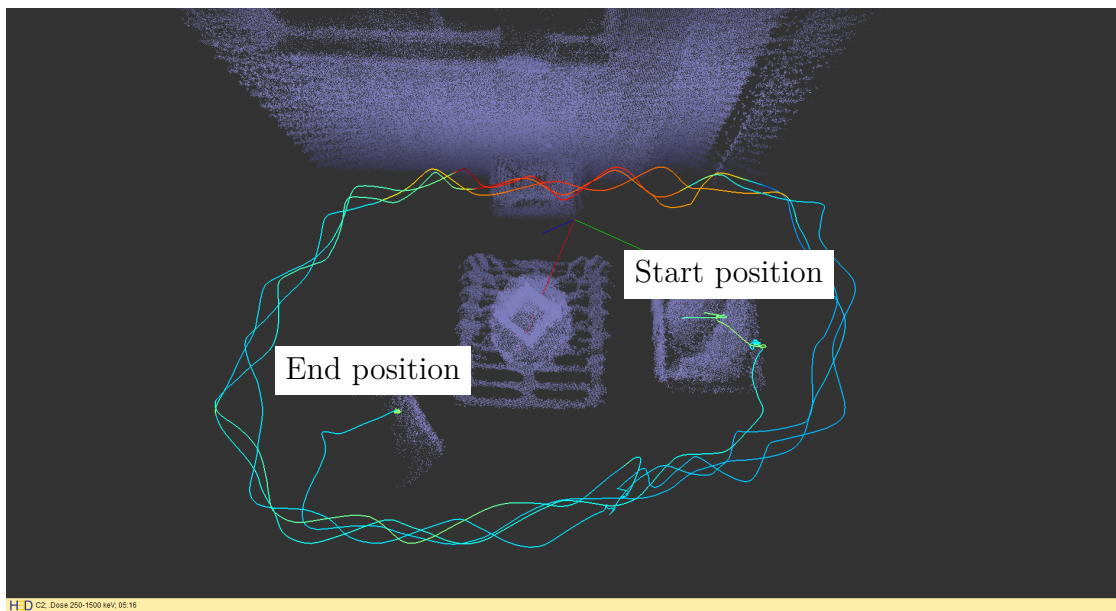


Figure 4.11: Path followed by the operator during the third and final scan. The starting and ending points, the latter near Luggage No. 3, are labelled. The colour-coded heat map is scaled to a peak dose rate of 400 nSv/h.

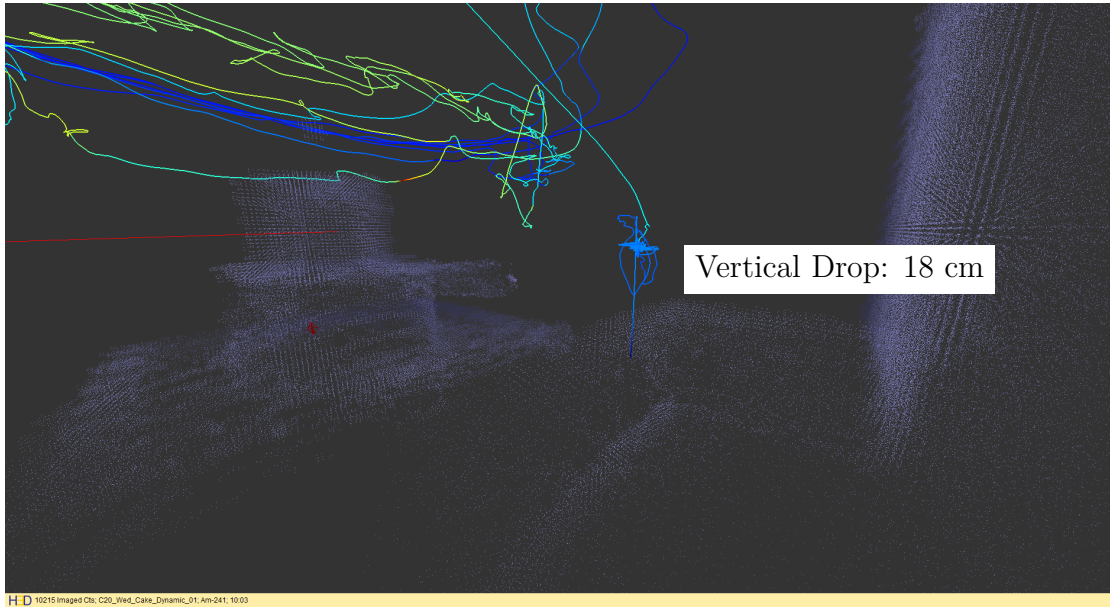


Figure 4.12: Detail of the vertical drop in the Z-coordinate at the end of the first continuous scan. The label 'Vertical Drop: 18 cm' highlights the measured decrease from the initial to the final Z-coordinates.

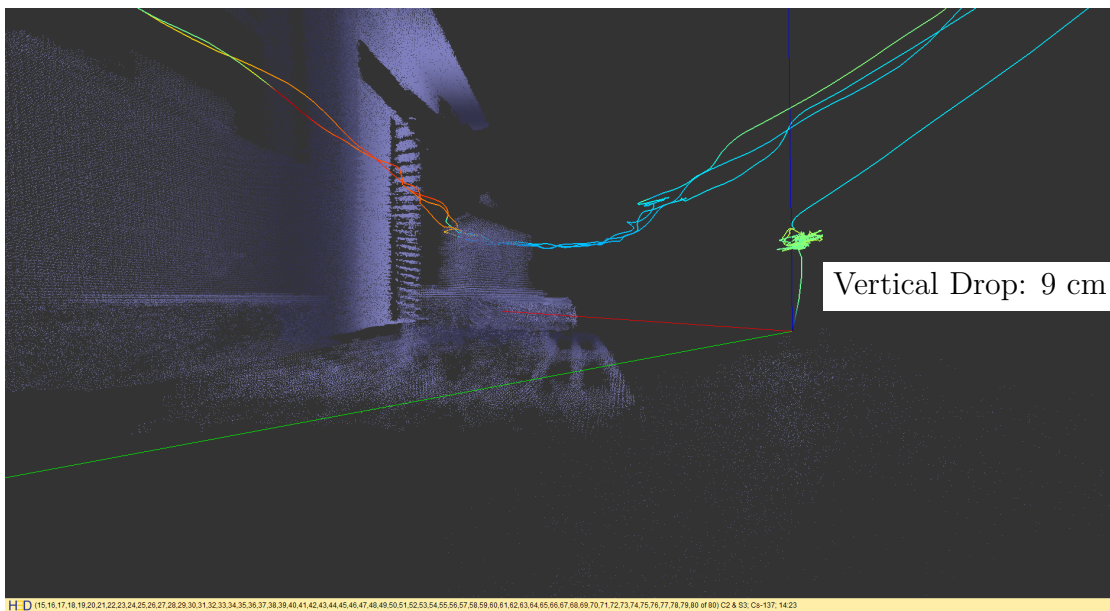


Figure 4.13: Detail of the vertical drop in the Z-coordinate at the conclusion of the last continuous scan. The label 'Vertical Drop: 9 cm' marks the change from the initial to the final Z-coordinates.

Chapter 5

Analysis and Results

The results presented in this chapter stem from the scanning procedures performed using two different systems: the 3D Mapper and the Tomographic Gamma Scanner (TGS). While the methodology for the 3D Mapper has been detailed in the previous section, the scanning procedure for the TGS will be described directly within this chapter, along with the corresponding qualitative and quantitative assessments of the acquired radiological data.

First, a qualitative analysis is conducted on the radiological clouds generated using the 3D Mapper (5.1), employing the Visualizer 3D software to evaluate both dynamic and combined dynamic and stationary measurements.

Next, a quantitative analysis is performed using CloudCompare (5.2), where specific geometric parameters are defined to compare the reconstructed cloud structures. The visual representation of source positions within these datasets is also explained.

The analysis then shifts to the TGS reconstructions, providing a qualitative interpretation of the retrieved source distributions (5.3) through a visual comparison of source positions.

Finally, the calculation of source extensions and quantitative error analysis (5.4) evaluates absolute, relative, and percentage errors (5.4.1), assessing the accuracy of the reconstructed positions (5.4.2). This section concludes with a discussion on the estimation of source extensions (5.4.3).

5.1 Qualitative Analysis of Radiological Clouds Generated with 3D Mapper

Stationary Scan Analysis

Stationary measurements were taken from fixed positions, allowing for an assessment of the gamma-ray emissions from a static perspective. Unlike continuous scans,

stationary scans lack depth perception, meaning only the two-dimensional origin of the radiation could be determined. This limitation results in the visualisation of the sources as conical projections extending downward into the ground (Figures 5.1, 5.2, and 5.3). The apparent penetration effect is a direct consequence of the inability to resolve the depth of the emission points. Despite this, the stationary scans provide valuable insights into the angular distribution of the detected radiation, highlighting the primary emission zones within the WC structure.

Combined Stationary-Continuous Scans

The integration of continuous and stationary scans was crucial for refining the spatial accuracy of the source positioning. Continuous scans contributed essential three-dimensional information, delineating the exact boundaries of the sources and resolving their depth within the WC. The three-dimensional reconstruction obtained from these measurements significantly enhanced the clarity of the results, allowing for a more precise identification of the radioactive sources within the object. The effectiveness of this combination is clearly visible in Figures 5.1d, 5.2d, and 5.3d, where the transition from individual stationary reconstructions (Figures 5.1a-c, 5.2a-c, 5.3a-c) to the enhanced combined image demonstrates improved localisation and intensity distribution.

Dynamic Scan and Comparison with TGS

Figures 5.4 showcase the Full Voxelisation reconstructions of ^{241}Am in SD, and ^{60}Co and ^{137}Cs in HD, based solely on the first dynamic measurement performed. This scan is particularly relevant to this study as it provides the dataset chosen for a direct comparison with the static TGS one. The first dynamic measurement enabled an initial three-dimensional reconstruction without integrating additional stationary scans.

Caesium Source Reconstruction Issues

During data analysis, particular challenges were noted concerning the caesium source located in the source box on the window ledge. The presence of this secondary source, illustrated in Figure 5.5, complicated the reconstruction, as its emissions interfered with the detection of the primary caesium source within the WC. This is demonstrated in Figure 5.3a, where the reconstruction is biased towards the source box, and in Figure 5.3b, where the reconstruction is split between the WC and the source box. This highlights that increasing the distance from the source box mitigates its influence, allowing the reconstruction to predominantly detect the caesium source within the WC, as observed in Figure 5.3c.

However, through optimised reprocessing in the Visualizer 3D software, a clear distinction between the two sources was achieved. The predominant source in the final reconstructions corresponds to the caesium within the WC rather than the one enclosed in its lead container in the source box, as illustrated in Figure 5.4c. This confirms the high capability of the system in differentiating spatially separated sources, as demonstrated when intensity thresholds were adjusted to reveal lower

radiation levels. In such cases, the reconstructed caesium source aligned accurately with its expected position within the WC structure (Figure 5.4d).

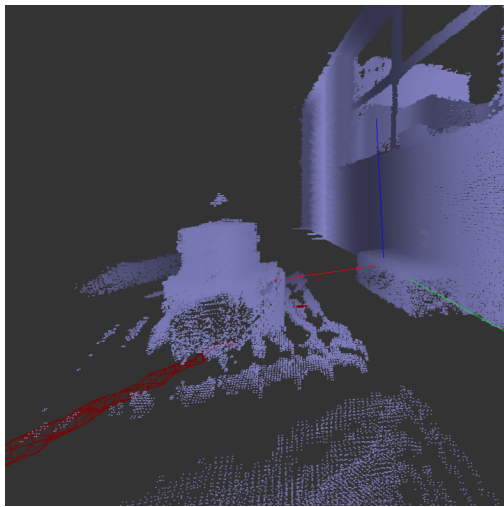
Interference Effects of Tungsten Fluorescence on ^{241}Am Detection

During the measurement of the the americium source using the CZT detector equipped with a tungsten mask, a variation in counting statistics was observed. This variation can be attributed to the presence of mid-to-high energy gamma-rays (in the range of 300–400 keV), primarily originating from the emissions of nearby ^{60}Co and ^{137}Cs sources. When these higher-energy gamma rays interact with the tungsten material of the collimator, they induce secondary fluorescence. This interaction leads to the emission of characteristic X-rays from the tungsten atoms, typically around 58 keV. These X-rays interfere with the detection of the ^{241}Am gamma peak, which occurs at 59.5 keV [21]. The overlap between the tungsten fluorescence and the ^{241}Am signal significantly reduces the signal-to-noise ratio, making accurate detection and reconstruction of the americium source particularly challenging. Future detector designs may incorporate a cadmium liner inside the collimator to absorb these characteristic X-rays from tungsten without significantly affecting the detection efficiency of americium’s gamma rays. Cadmium, with its high absorption cross-section for low-energy photons, would help mitigate this interference, thereby improving the accuracy and reliability of americium measurements [19].

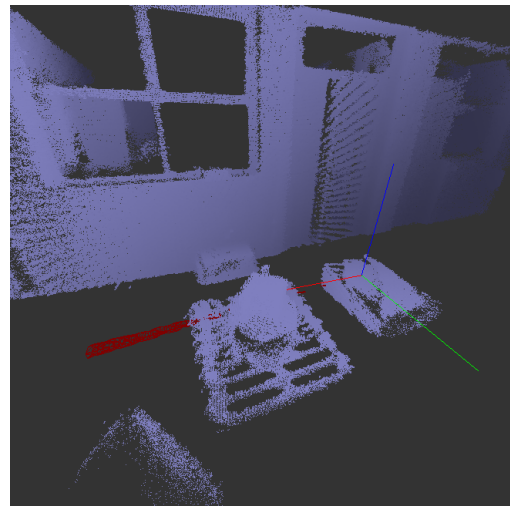
Addressing the Z-Coordinate Drop Issue

A previously discussed software-related issue affected the Z-coordinate stability, particularly evident in stationary scans performed from fixed positions. This problem was most noticeable in the first stationary scan, conducted from above Luggage No. 1, where the reconstructed source locations appeared misaligned due to the erroneous altitude shift. The discrepancy in the vertical positioning of the first stationary scan, compared to those performed at Luggage No. 2 and Luggage No. 3, further illustrated the impact of this software anomaly. However, the integration of continuous scans mitigated this issue, as their dynamic nature allowed for a more accurate recalibration of the system’s true spatial positioning.

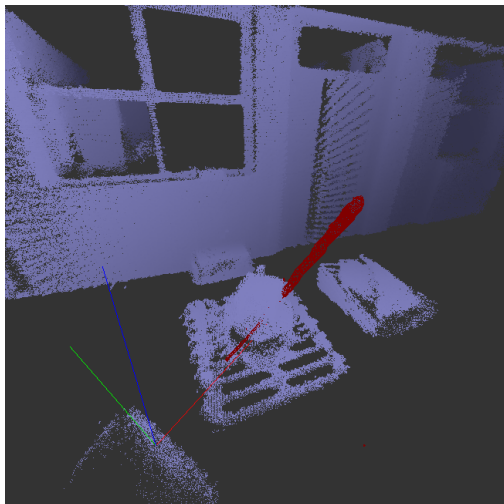
Overall, the combination of continuous and stationary scans proved essential in overcoming the inherent limitations of static measurements while ensuring precise three-dimensional source localisation within the WC.



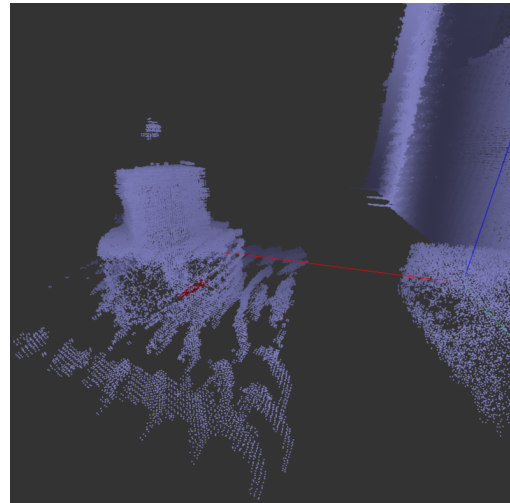
(a) ^{241}Am SD 1st measurement



(b) ^{241}Am SD 2nd measurement

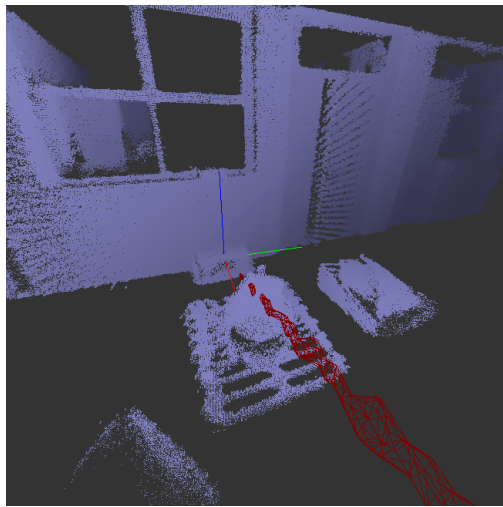


(c) ^{241}Am SD 3rd measurement

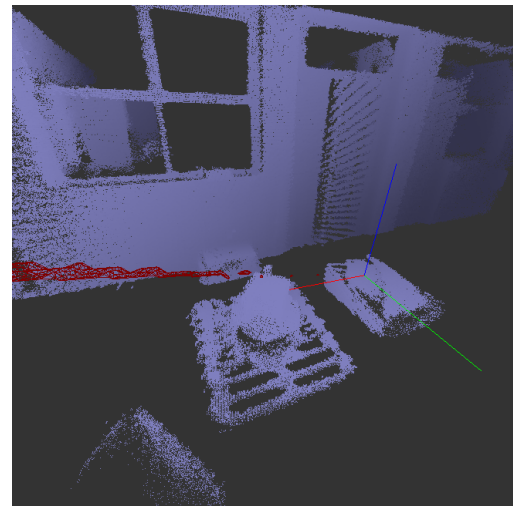


(d) ^{241}Am SD Combined reconstruction

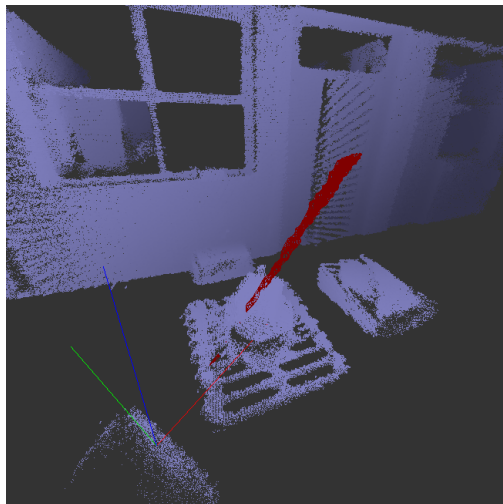
Figure 5.1: 3D reconstruction of the ^{241}Am source using the SD Full Voxelisation Reconstruction mode from Visualizer 3D. The first three images (a-c) represent the three individual stationary measurements, while the last image (d) shows the combined reconstruction from all six measurements, integrating stationary and continuous scans.



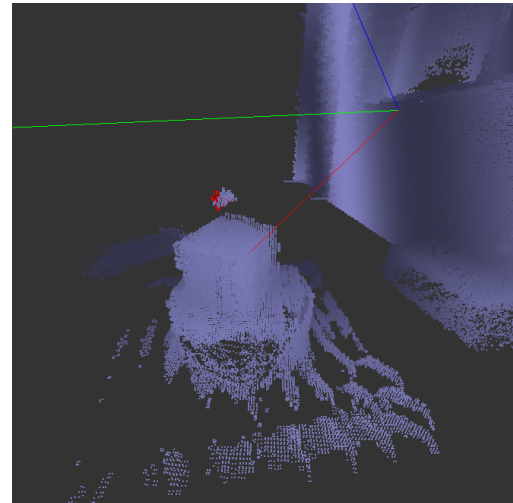
(a) ^{60}Co HD 1st measurement



(b) ^{60}Co HD 2nd measurement

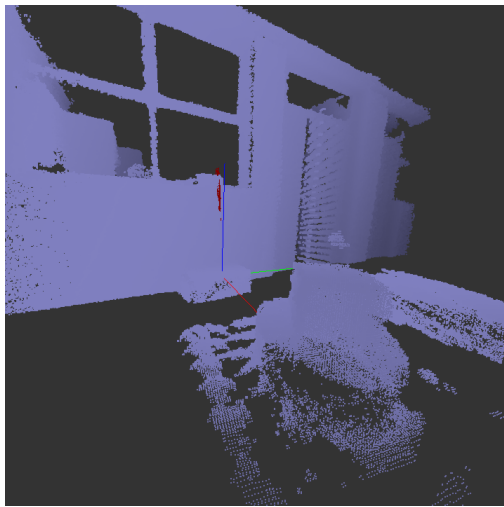


(c) ^{60}Co HD 3rd measurement

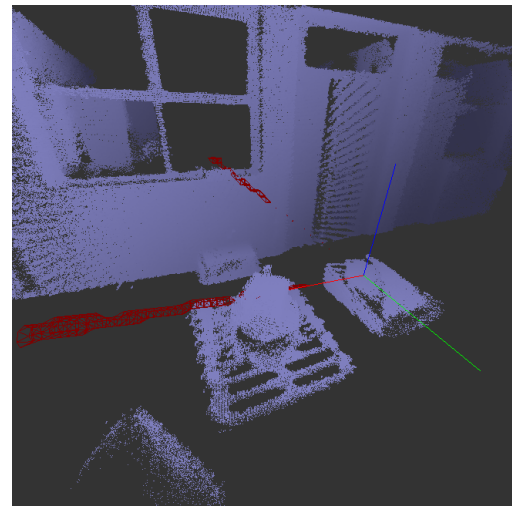


(d) ^{60}Co HD Combined reconstruction

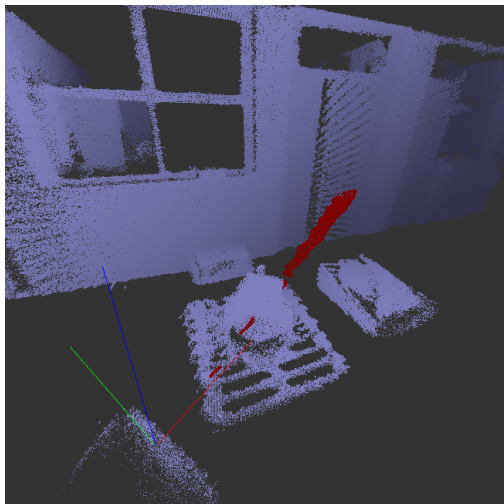
Figure 5.2: 3D reconstruction of the ^{60}Co source using the HD Full Voxelisation Reconstruction mode. The first three images (a-c) correspond to the individual stationary measurements, while the last image (d) shows the combined reconstruction from all six measurements, integrating stationary and continuous scans.



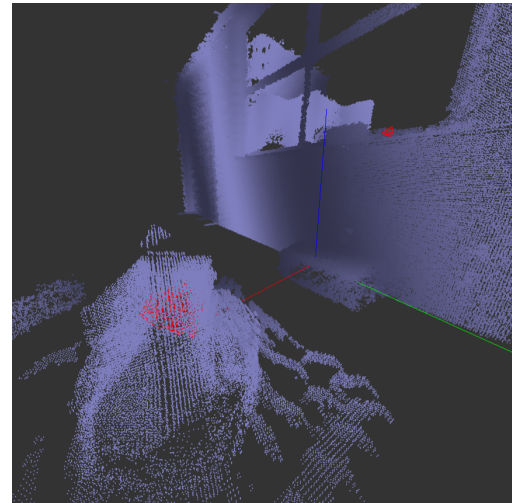
(a) ^{137}Cs HD 1st measurement



(b) ^{137}Cs HD 2nd measurement

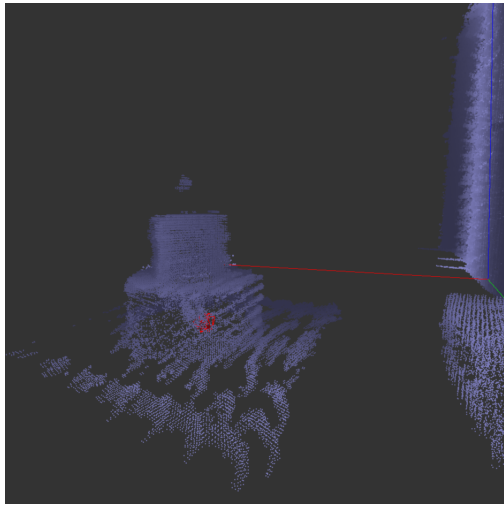


(c) ^{137}Cs HD 3rd measurement

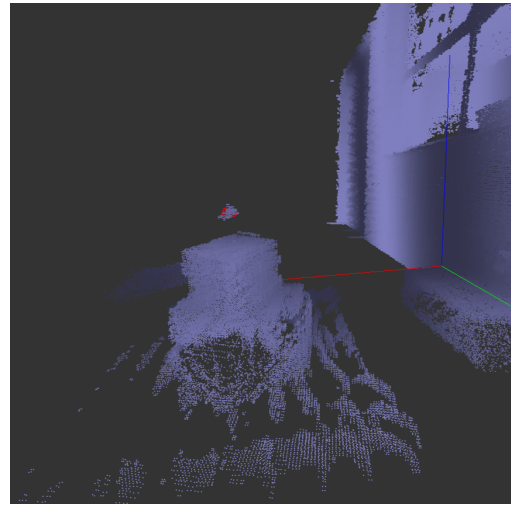


(d) ^{137}Cs HD Combined reconstruction

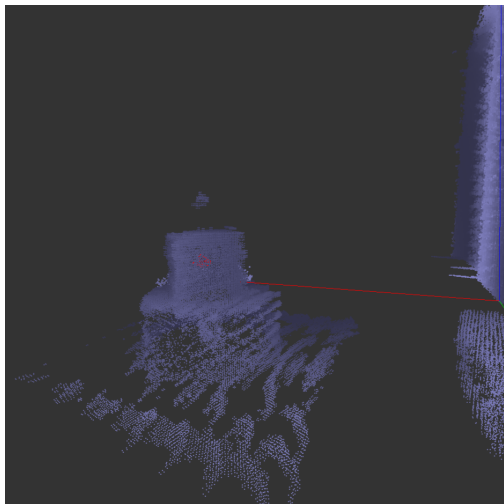
Figure 5.3: 3D reconstruction of the ^{137}Cs source using the HD Full Voxelisation Reconstruction mode. The first three images (a-c) correspond to the individual stationary measurements, while the last image (d) shows the combined reconstruction from all six measurements, integrating stationary and continuous scans.



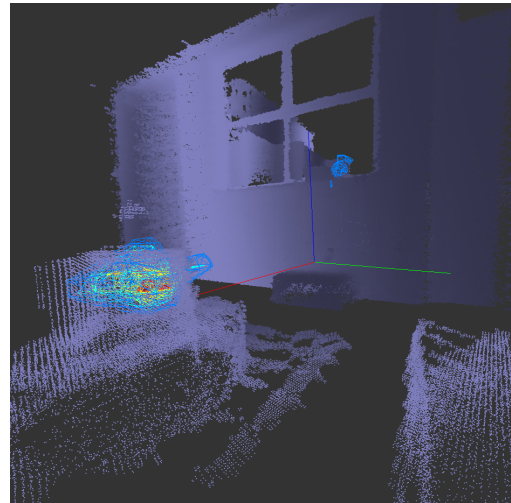
(a) ^{241}Am SD reconstruction



(b) ^{60}Co HD reconstruction



(c) ^{137}Cs HD reconstruction



(d) ^{137}Cs HD with lowered algorithm threshold.

Figure 5.4: 3D reconstruction of test sources in SD and HD Full Voxelisation modes using Visualizer 3D. Images (a) to (c) depict individual source reconstructions obtained from the first dynamic measurement, which is the only dataset compared to the TGS. Image (d) shows the enhanced reconstruction of (c), with a lowered algorithm threshold to reveal additional hotspots, including ^{137}Cs within the box.



Figure 5.5: Box containing the protective cases for the sources used in the study. Two ^{137}Cs sources, still inside their sealed containers, were left on the window ledge. Their larger size prevented their use in the experiment, but their proximity to the setup caused an unintended contribution to the radiation measurements.

5.2 Quantitative Analysis Using CloudCompare

Definition of Invariant Parameters for Geometric Comparison

To accurately compare the spatial positioning of each radioactive source within the reconstructed geometry, two primary geometric parameters were defined at the outset:

Radial Distance (r):

The horizontal distance from the predefined origin to the point with the highest measured intensity.

Vertical Distance (z):

The height of the point with the highest detected intensity relative to the origin.

The *origin* was consistently set at the centre of the top surface of the Marinelli beaker, ensuring a stable reference for all distance measurements. Unlike bottom-up measurements, all distances were considered from the top downwards, preventing inconsistencies due to the hollow nature of the WC reconstruction.

Point Cloud Processing and Mesh Generation in CloudCompare

The dataset from the first dynamic scan was imported from Visualizer 3D into CloudCompare for further refinement. Before generating the mesh, a filtering step was performed to exclude points associated with intensities below a set threshold. This selection process, similar to the threshold selection in Visualizer 3D, drastically reduced the number of points available for processing. Consequently, this reduction introduced challenges in mesh generation, as a lower point density limited the continuity of the reconstructed surfaces.

To mitigate these limitations, a *solid mesh* was initially generated using Delaunay 2.5D triangulation algorithm [42]. However, this representation significantly differed from the mesh produced in Visualizer 3D (Figure 5.4).

The final reconstructed solids, encircled in azure in Figure 5.6, are displayed individually in Figures 5.7, 5.8, and 5.9. Distances from the predefined origin are marked in purple in Figure 5.6 and in red in the other three figures.

In Figure 5.10, a *wireframe mesh* is presented, which more closely resembles the one generated by the Visualizer 3D. However, this type of representation complicates visual comparison, as the lack of surface continuity hinders the clear identification of spatial relationships and intensity distribution.

The calculated distances for each source, obtained from the defined origin, are summarised in Table 5.1. These values will serve as reference points in the comparative analysis with the TGS system.

Table 5.1: Measured distances of radioactive sources from the defined origin. These values will be used for comparison with the TGS system.

Source	Radial Distance [cm]	Vertical Distance [cm]
^{241}Am	19.0	65.5
^{60}Co	3.4	10.5
^{137}Cs	4.2	35.5

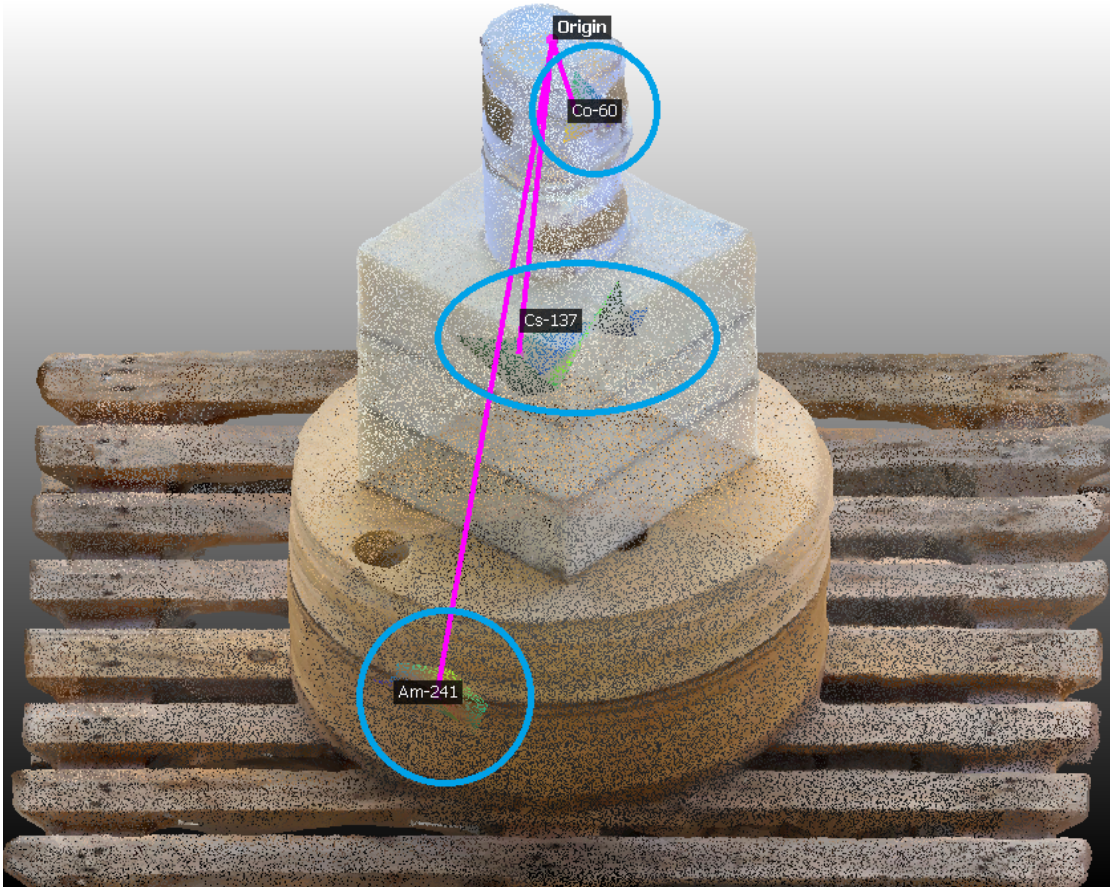


Figure 5.6: Complete lateral view of the ^{241}Am , ^{60}Co , and ^{137}Cs reconstructions as solid meshes, encircled in azure. Distances from the origin are marked in purple.

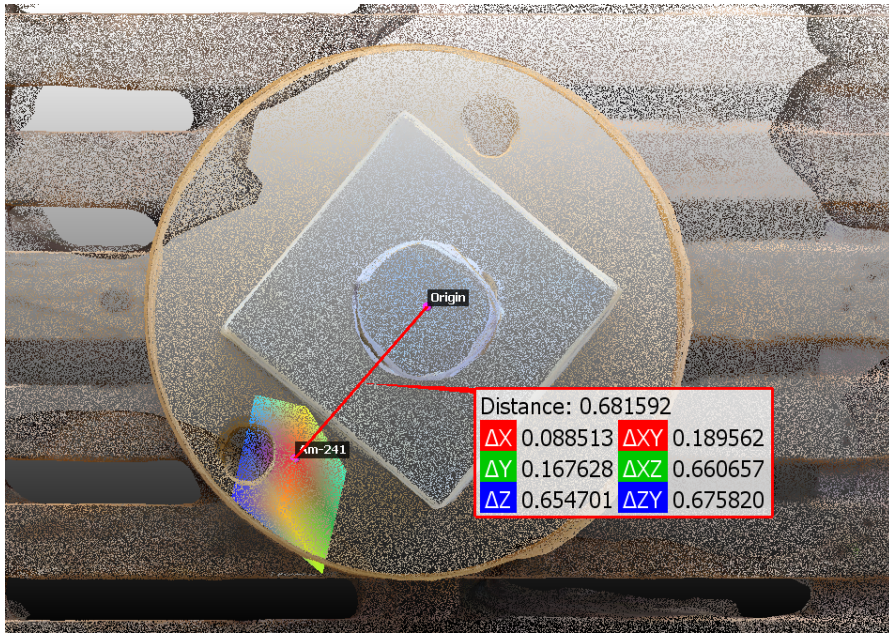


Figure 5.7: Top view of the ^{241}Am source reconstruction in CloudCompare, using a solid mesh representation.

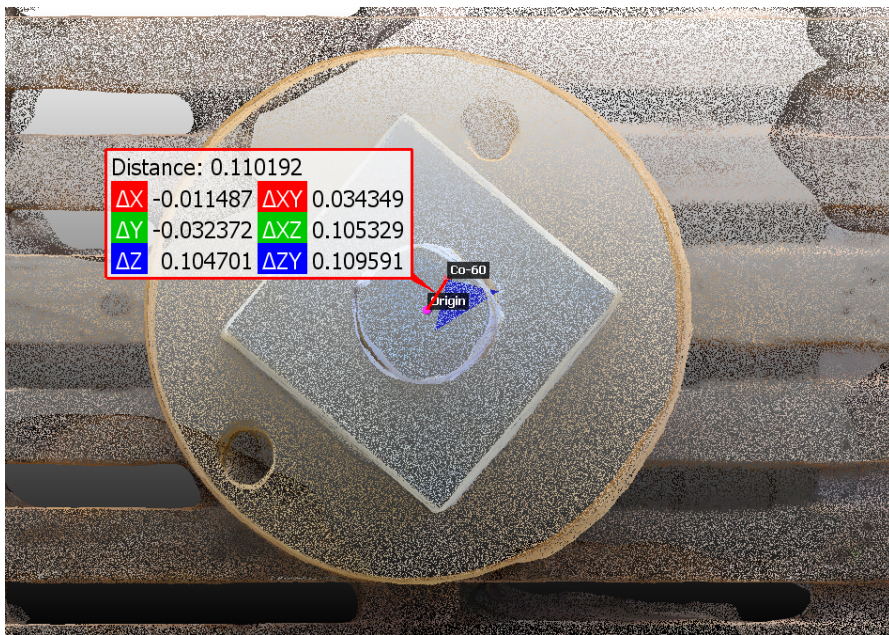


Figure 5.8: Top view of the ^{60}Co source reconstruction in CloudCompare, using a solid mesh representation.

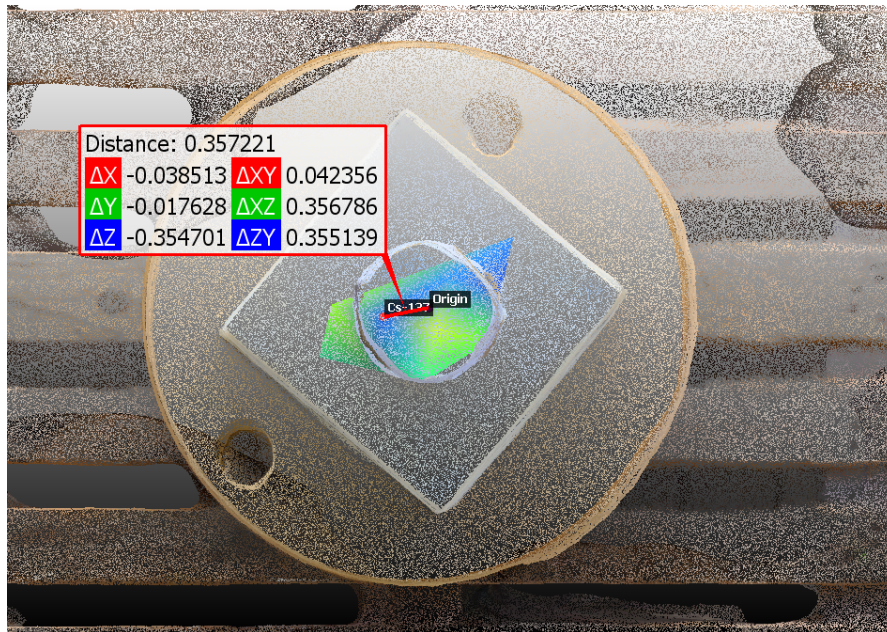


Figure 5.9: Top view of the ^{137}Cs source reconstruction in CloudCompare, using a solid mesh representation.

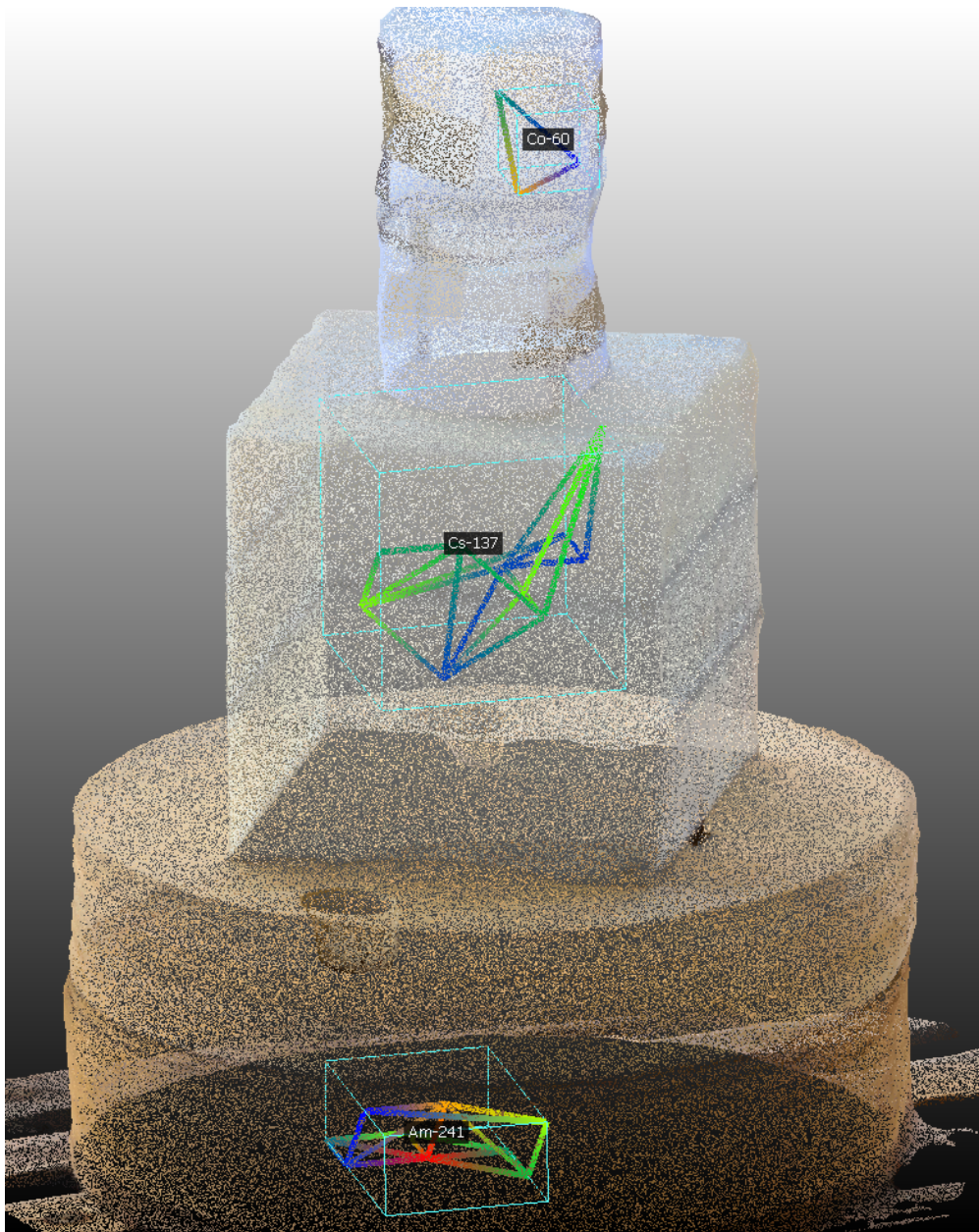


Figure 5.10: Wireframe mesh visualisations generated in CloudCompare for the reconstructed radioactive sources ^{241}Am , ^{60}Co , and ^{137}Cs . These visualisations closely resemble those displayed in Visualizer 3D. The bounding boxes, highlighted in light blue, will be used later for studying the extents of the sources.

5.3 Qualitative Analysis of TGS Reconstructions

Visual Representation of Source Positions

The following Figures 5.11, 5.12 and 5.13 present the reconstruction of the three sources using the TGS. The images (a-c) correspond to different plane views selected via the TGS Viewer software in conjunction with the peak intensity value. Consequently, the planes shown are not the same for all three sources but are specific to each one. This method facilitated the recognition of the source positions.

The reconstruction process involves two complementary imaging techniques: transmission and emission imaging. Transmission imaging is performed using the Algebraic Reconstruction Technique (ART), which is well-suited for dense materials and heterogeneous matrices [27]. This algorithm iteratively refines voxel values to achieve consistency with the measured data, ensuring accurate attenuation mapping. Emission imaging, on the other hand, is carried out using the Maximum Likelihood Expectation Maximization (MLEM) algorithm. MLEM iterates towards the most likely spatial distribution of gamma-emitting sources by leveraging statistical modelling, thus enhancing image quality even in low-count scenarios. The Non-Negative Least Squares (NNLS) algorithm has not been used as a preliminary step before the MLEM one, it ensures non-negative voxel values during reconstruction, preventing non-physical results.

In addition to the individual sectional views, Figure 5.14 presents a complete 3D reconstruction of the three sources within the WC, providing an overall spatial representation of their relative positions. This 3D view will serve as a key reference for the comparative analysis between the TGS and 3D Mapper systems, enabling an assessment of the differences in the results obtained with the two reconstruction methods.

To estimate the spatial position of the radioactive sources within the TGS reconstructions, a method analogous to that employed in CloudCompare was adopted. The reference origin was defined based on the symmetrical structure visible in the Y-Z plane within the TGS Viewer. The origin was selected along the rotation axis of the solid at the height corresponding to the top edge of the Marinelli beaker. This symmetry, clearly illustrated in Figure 5.15, facilitated the consistent identification of the origin across all planes.

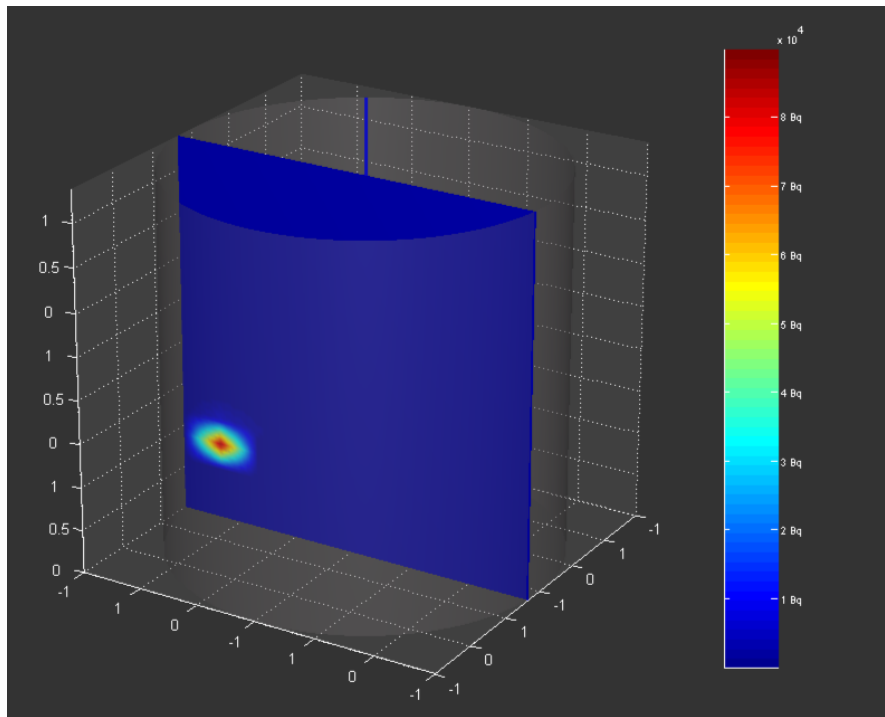
The radial distance (r) was determined by measuring the horizontal displacement from the defined origin to the point of peak activity visible in the XY plane. Similarly, the vertical distance (z) was assessed by analysing the position of maximum intensity along the Z-axis, as seen in both the Y-Z and X-Z planes. This approach mirrors the strategy applied using CloudCompare, where the distances were calculated from the origin to the points with the highest intensity prior to mesh generation.

This method was adopted to ensure consistency in the comparison between the TGS and 3D Mapper results. While some differences may still arise due to variations in spatial resolution, voxel size, or reconstruction algorithms, using a common and symmetrical reference framework helps minimise discrepancies related to differing measurement setups.

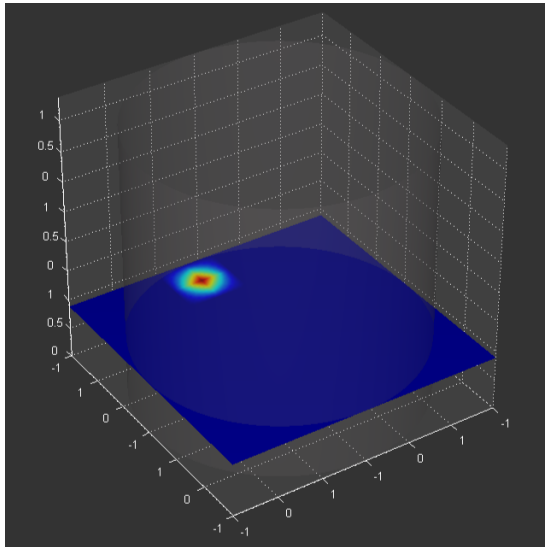
The measured distances for each source, calculated from the origin, are summarised in Table (5.2).

Table 5.2: Measured distances of radioactive sources from the defined origin using the TGS system. These values will be compared with those obtained from 3D Mapper.

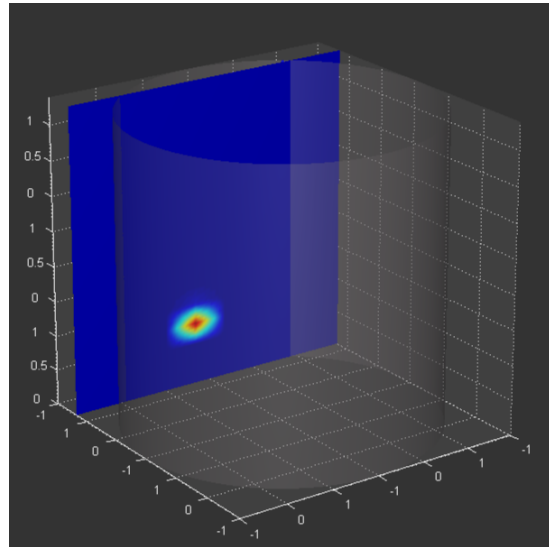
Source	Radial Distance [cm]	Vertical Distance [cm]
^{241}Am	20.2	66.3
^{60}Co	3.5	10.8
^{137}Cs	4.3	35.9



(a) ^{241}Am TGS Reconstruction on Y-Z plane with colour scale.

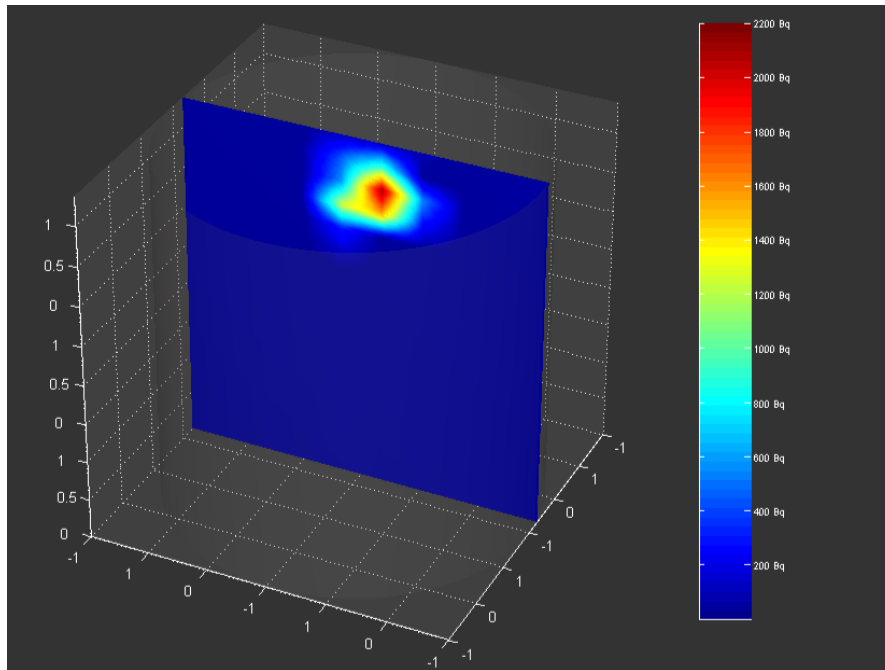


(b) ^{241}Am TGS Reconstruction on X-Y plane.

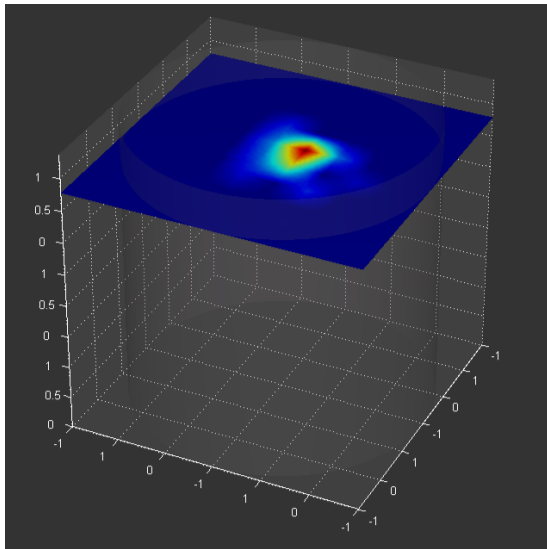


(c) ^{241}Am TGS Reconstruction on X-Z plane.

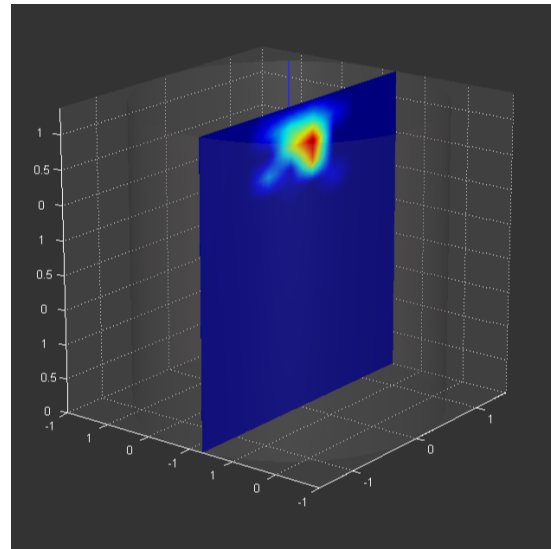
Figure 5.11: Reconstruction of the ^{241}Am source using the TGS. The images (a-c) correspond to the different planes view. Image (a) also shows the colour scale for the activity intensity.



(a) ^{60}Co TGS Reconstruction on Y-Z plane with colour scale.

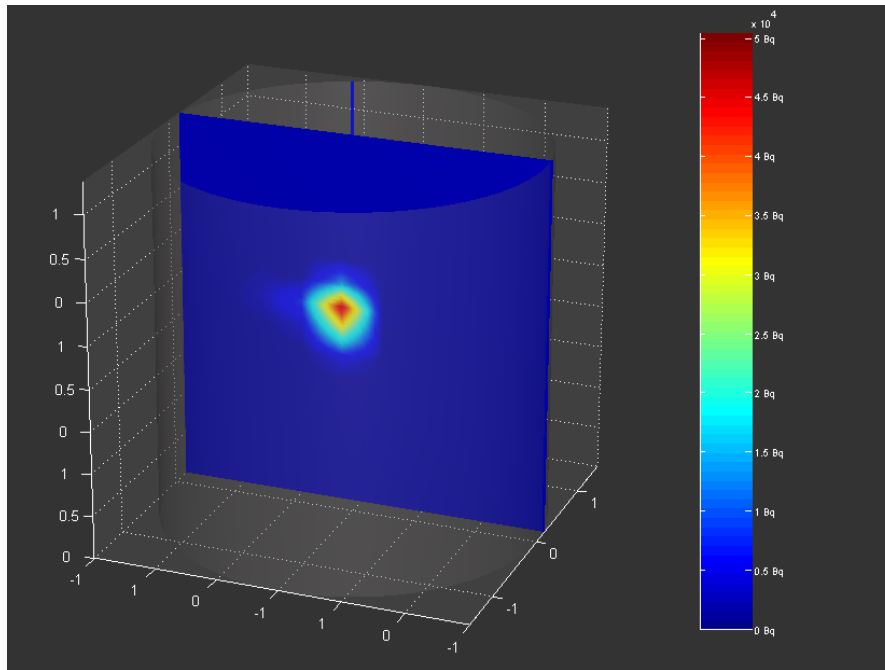


(b) ^{60}Co TGS Reconstruction on X-Y plane.

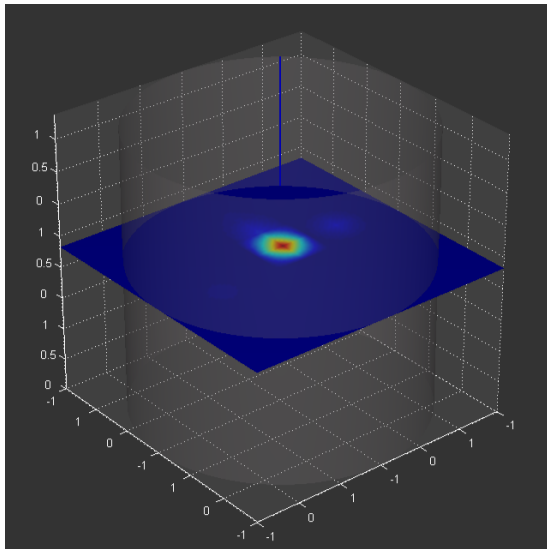


(c) ^{60}Co TGS Reconstruction on X-Z plane.

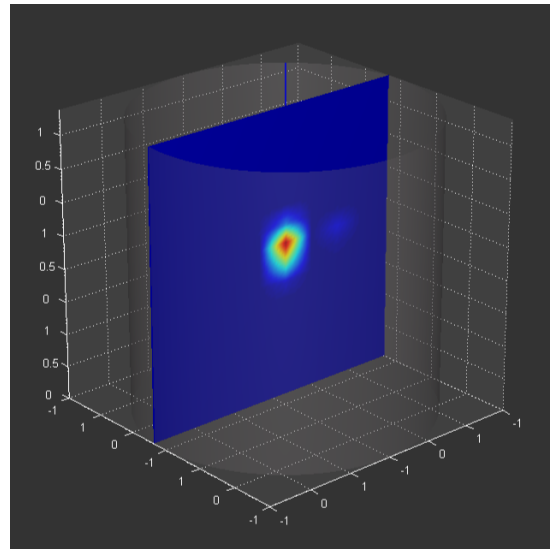
Figure 5.12: Reconstruction of the ^{60}Co source using the TGS. The images (a-c) correspond to the different planes view. Image (a) also shows the colour scale for the activity intensity.



(a) ^{137}Cs TGS Reconstruction on Y-Z plane with colour scale.

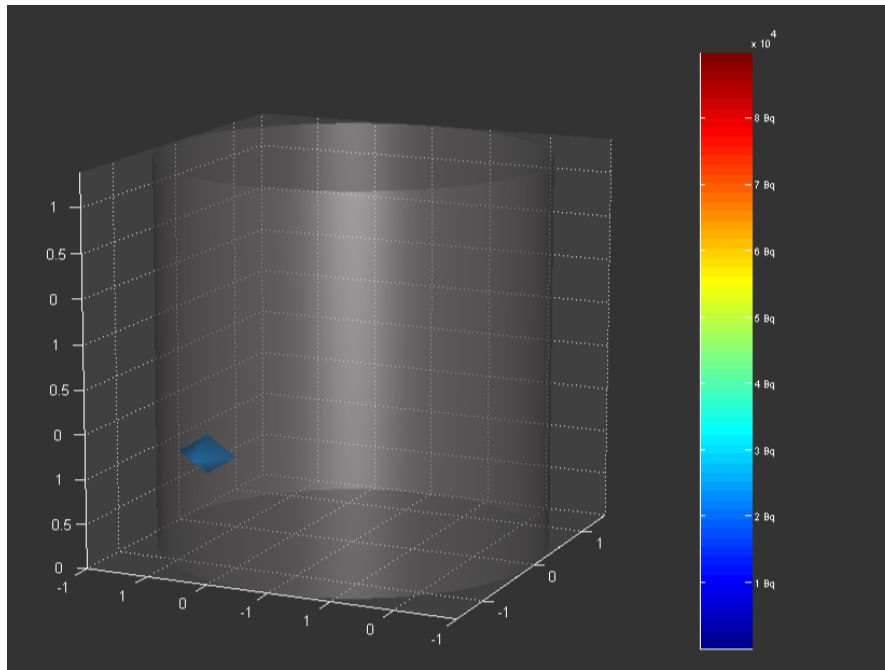


(b) ^{137}Cs TGS Reconstruction on X-Y plane.

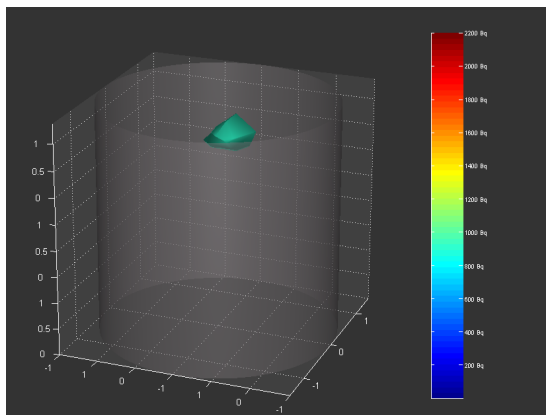


(c) ^{137}Cs TGS Reconstruction on X-Z plane.

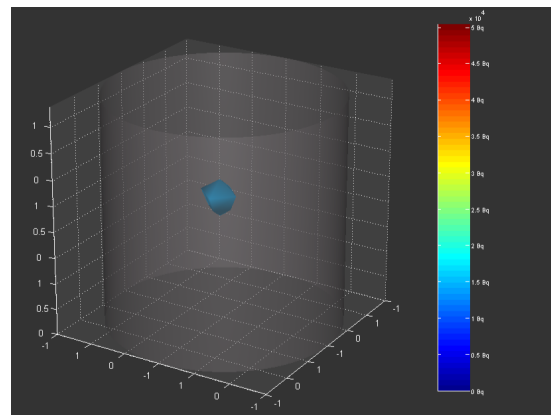
Figure 5.13: Reconstruction of the ^{137}Cs source using the TGS. The images (a-c) correspond to the different planes view. Image (a) also shows the colour scale for the activity intensity.



(a) ^{241}Am TGS 3D Reconstruction.



(c) ^{60}Co TGS 3D Reconstruction.



(d) ^{137}Cs TGS 3D Reconstruction.

Figure 5.14: 3D Reconstruction of the (a) ^{241}Am , (b) ^{60}Co and (c) ^{137}Cs sources using the TGS. The images also show the colour scale for the activity intensity.

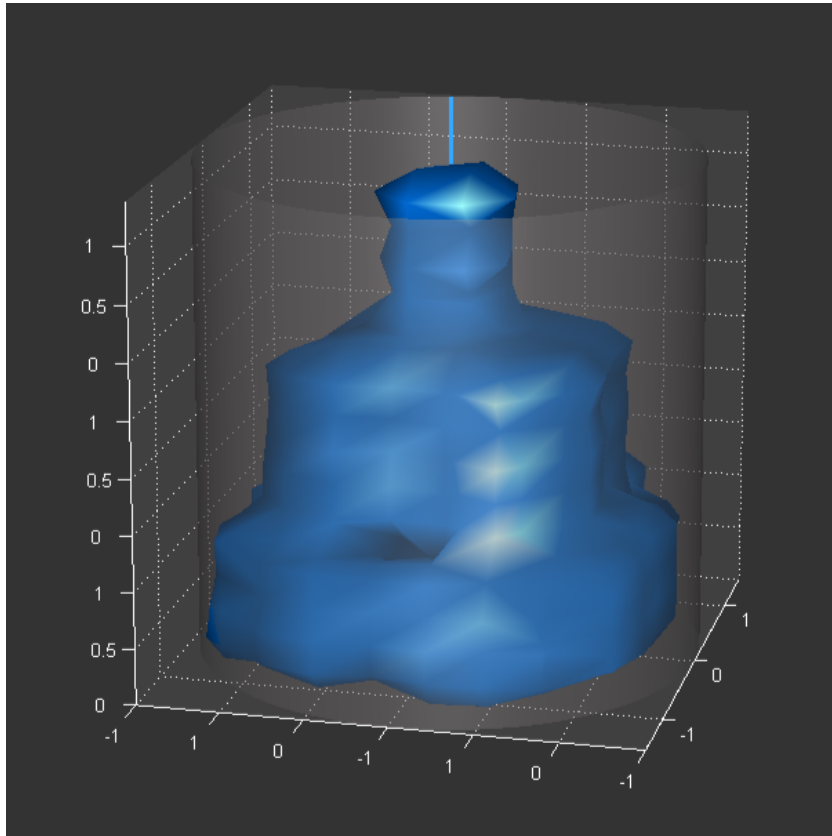


Figure 5.15: 3D matrix reconstruction of the WC geometry as visualised in the TGS Viewer. The symmetry of the structure along the central axis facilitated the selection of a consistent reference origin for spatial measurements. The surface at the top aligns with the upper boundary of the Marinelli beaker, which served as the vertical reference point for calculating radial and vertical distances.

5.4 Calculation of Source Extensions and Quantitative Error Analysis

To estimate the spatial extent of the reconstructed sources, two key parameters were considered: radial extension and vertical height. These measurements offer a clear and straightforward understanding of the source dimensions.

For the **3D Mapper**, the point cloud data relative to the three sources were enclosed within bounding boxes automatically generated by the software. These boxes defined the dimensions of each source along the X -, Y -, and Z -axes, as shown in Figure 5.10. The radial extension was determined by averaging the

lengths along the X - and Y -axes, while the vertical height corresponded directly to the measurement along the Z -axis. This method provides a clear geometric representation of each source's size.

For the **Tomographic Gamma Scanner (TGS)**, the source dimensions were directly estimated from the visualisation of the reconstructed activity distributions along the X -, Y -, and Z -axes. The radial extension was calculated by measuring the horizontal spread of activity relative to the central axis (the origin), while the vertical height was measured from the top surface of the Marinelli beaker down to the lowest point of detectable activity. This approach was designed to align with the methodology used for 3D Mapper, ensuring consistency in the comparison.

Once the measurements were obtained, a comparison was made to assess the consistency between the two systems.

Table 5.3 compares the radial extensions and heights of the sources as measured by both 3D Mapper (3DM) and the Tomographic Gamma Scanner (TGS). The radial extension refers to the maximum horizontal spread of the detected activity, while the vertical height corresponds to the spread along the Z -axis.

Table 5.3: Comparison of source dimensions between 3D Mapper (3DM) and Tomographic Gamma Scanner (TGS).

Source	Method	Radial Extension [cm]	Height [cm]
^{241}Am	TGS	12.8	5.0
	3DM	18.0	5.0
^{60}Co	TGS	15.0	7.0
	3DM	7.1	5.0
^{137}Cs	TGS	18.0	6.0
	3DM	21.2	15.0

5.4.1 Quantitative Error Analysis

To compare the accuracy of the Tomographic Gamma Scanner (TGS) and 3D Mapper (3DM) systems, three different error metrics were considered: absolute error, relative error, and percentage error. These metrics were calculated for both the radial extension and height of the sources.

Absolute Error

The absolute error (E_a) was calculated using the formula:

$$E_a = |\text{TGS value} - \text{3DM value}| \quad (5.1)$$

Relative Error

The relative error (E_r) was calculated using the formula:

$$E_r = \frac{|\text{TGS value} - \text{3DM value}|}{\text{TGS value}} \quad (5.2)$$

Percentage Error

The percentage error (E_p) was calculated as:

$$E_p = \left(\frac{|\text{TGS value} - \text{3DM value}|}{\text{TGS value}} \right) \times 100 \quad (5.3)$$

Table 5.4: Error analysis for source extensions (radial extension and height) between 3D Mapper (3DM) and Tomographic Gamma Scanner (TGS).

Source	Extension Type	Absolute Error [cm]	Relative Error [%]
²⁴¹ Am	Radial	5.2	41%
	Height	0.0	0%
⁶⁰ Co	Radial	7.9	53%
	Height	2.0	29%
¹³⁷ Cs	Radial	3.2	16%
	Height	9.0	67%

Table 5.5: Error analysis of source distances from the defined origin between 3D Mapper (3DM) and Tomographic Gamma Scanner (TGS).

Source	Distance Type	Absolute Error [cm]	Relative Error [%]
²⁴¹ Am	Radial	1.2	6%
	Vertical	0.8	1%
⁶⁰ Co	Radial	0.1	2%
	Vertical	0.3	3%
¹³⁷ Cs	Radial	0.1	1%
	Vertical	0.4	1%

5.4.2 Reconstructed Positions

Table 5.6: Comparison of source distances from the defined origin between 3D Mapper (3DM) and Tomographic Gamma Scanner (TGS).

Source	Method	Radial Distance [cm]	Vertical Distance [cm]
²⁴¹ Am	TGS	20.2	66.3
	3DM	19.0	65.5
⁶⁰ Co	TGS	3.5	10.8
	3DM	3.4	10.5
¹³⁷ Cs	TGS	4.3	35.9
	3DM	4.2	35.5

The reconstructed positions (illustrated in Table (5.6)) obtained from both systems demonstrate excellent agreement, considering the numerous approximations involved due to the extensive data processing. Despite the initial data not constituting a statistically significant sample, the results are noteworthy. The height of the sources, measured from top to bottom, aligns with the expected values for all three sources, which are highlighted in Table 5.7.

For **Americium**, positioned in a 10 cm deep hole in the wooden part of the WC, the expected height is approximately 66 cm, with a radial distance from the origin of about 18.5 cm.

Table 5.7: Expected distances of radioactive sources from the defined origin based on the known positioning within the WC geometry.

Source	Radial Distance [cm]	Vertical Distance [cm]
^{241}Am	18.5	66.0
^{60}Co	0.0	13.0
^{137}Cs	0.0	37.0

For **Caesium**, the source, with a height of about 2 cm and positioned at 38 cm, should have a vertical distance from the origin between 36 and 38 cm.

For **Cobalt**, positioned between two Marinelli containers, each 13 cm tall, the expected vertical distance should be 13 cm.

However, the radial distances for cobalt and caesium differ from the expected values, despite their theoretical alignment along the axis of rotation. The similarity in data from both systems suggests human error rather than a reconstruction flaw.

5.4.3 Source Extensions

The data on source extensions revealed notable discrepancies between the two systems.

For the **TGS**, although the source was well-defined, allowing for a more consistent analysis, it is important to acknowledge that both the scanning process and the subsequent distance analysis have their own limitations. As with any algorithm, issues can arise due to challenging geometries. For instance, the upper plane of the first Marinelli, where the origin was fixed, is determined with a certain margin of error.

For the **3D Mapper**, several factors compromised the accuracy of the source extensions:

Measurement duration

The short duration affected the data quality.

External sources

The presence of additional sources interfered with the measurements.

Data processing

The extensive operations performed on the point cloud to obtain the necessary parameters introduced artefacts, leading to overly extended reconstructions.

These issues resulted in exaggerated extension values compared to those obtained from the Visualizer 3D reconstruction, indicating excessive reliance on software artefacts that distorted the reconstruction.

Chapter 6

Conclusions and Perspectives

The aim of this analysis was to conduct a series of measurements intended to validate the 3D Mapper in various contexts and applications. Unfortunately, the GammAware system, which is part of the 3D Mapper, broke down, likely due to a failure of the LIDAR component. This prevented further testing to address the issues identified during the analysis, limiting the study to the only available measurement.

The initial doubts about the reconstruction quality, caused by leaving the sources on the window ledge, eventually led to valuable discussions. This scenario demonstrated the instrument's capability to distinguish between different sources with varying distributions, and the quality of these reconstructions was notable. This experience highlights the importance of a *learning by doing* approach and the value of not discarding measurements.

Another important difference is that the tomography measurement was taken earlier in the process. These measurements were performed at different stages of the work, which means that some elements may have shifted slightly over time. Additionally, the Wedding Cake reference object was reconstructed, and it is highly likely that its positioning was not identical to the original setup.

From a technological standpoint, CZT detectors have proven to be excellent for this type of reconstruction. They operate at ambient temperature, which simplifies their use in various settings. Moreover, the latest CZT detectors offer performance levels that are relatively close to those of germanium detectors. Their versatility allows them to be mounted on drones and robot models, facilitating remote measurements.

On the other hand, the TGS system has confirmed its effectiveness in stationary applications. Its static scanning approach provides high spatial resolution and

accurate reconstructions, thanks to the HPGe detector, making it a reliable tool for precise spatial measurements.

Hardware Improvements

For the H420 detector, which features a tungsten mask, modifications are already planned, such as adding a cadmium liner to address the issue with americium, as described in the previous chapter (5.1). Regarding the GammAware system, it is reasonable to expect that advancements in optical and LIDAR technology will enable the replacement of current components with more advanced models. These new components could generate scenes with a higher number of points or even produce images for photogrammetric processing, integrating tailored algorithms to enhance data quality.

Additionally, recent advancements in HPGe cooling technology (used in the TGS detector) are aimed at reducing current limitations, paving the way for new HPGe detectors in portable gamma imaging applications. These detectors perform better in the study of plutonium and uranium, where the high number of peaks in the spectrum requires very advanced resolution. However, it must be noted that the industry is now focused on pixelated CZT technology, with the development of tailored algorithms. Finding an analogous solution for HPGe will require significant effort.

Software Enhancements

The integration of advanced point cloud management and measurement tools within the Visualizer 3D software could have prevented information loss. Future developments should focus on enhancing these capabilities to improve the accuracy of source extensions in dynamic scanning systems.

While the Iterative Closest Point (ICP) method was successfully employed for point cloud alignment in this study, alternative techniques such as feature-based alignment, available in CloudCompare, could be explored in future work. Different mesh generation methods could be considered to obtain comparable results between the two software systems. Implementing and testing these alternative methods on future datasets could enhance automation and reduce the reliance on manual preprocessing.

Bibliography

- [1] Syed N. Ahmed. *Physics and Engineering of Radiation Detection*. First. Elsevier, 2007.
- [2] Jacob Shapiro. *Radiation Protection*. Fourth. Harvard University Press, 2002.
- [3] Glenn F. Knoll. *Radiation Detection and Measurement*. Fourth. Wiley, 2010.
- [4] International Commission on Radiological Protection (ICRP). *Compendium of Dose Coefficients based on ICRP Publication 60*. Vol. 41. ICRP Publication 119 Suppl. Annals of the ICRP, 2012.
- [5] Repubblica Italiana. *Legge 11 settembre 2020, n. 120 - Conversione in legge, con modificazioni, del decreto-legge 16 luglio 2020, n. 76, recante misure urgenti per la semplificazione e l'innovazione digitale*. 2020. URL: <https://www.gazzettaufficiale.it/eli/id/2020/08/12/20G00121/sg>.
- [6] Nicholas Tsoulfanidis and Sheldon Landsberger. *Measurement and Detection of Radiation*. Fifth. CRC Press, 2021.
- [7] Frank H. Attix. *Introduction to Radiological Physics and Radiation Dosimetry*. First. Wiley-VCH, 2004.
- [8] Raymond Murray and Keith E. Holbert. *Nuclear Energy: An Introduction to the Concepts, Systems, and Applications of Nuclear Processes*. Eighth. Elsevier, 2019.
- [9] Manuel García-León. *Detecting Environmental Radioactivity*. Springer International Publishing, 2022.
- [10] Texas A&M University. *Basic Radiation Detection*. Accessed: 2024-09-10. Nuclear Security & Safeguards Education Portal (NSSEP), Center for Nuclear Security Science and Policy Initiatives (NSSPI). URL: <https://nsspi.tamu.edu/nssep/basic-nuclear-science-courses/basic-radiation-detection>.
- [11] Páll Theodórsson. *Measurement of Weak Radioactivity*. World Scientific, 1996.

-
- [12] Ortec. *High-Purity Germanium (HPGe) Radiation Detectors: Detector Cooling*. Accessed: 2025-02-14. URL: <https://www.ortec-online.com/products/radiation-detectors/high-purity-germanium-hpge-radiation-detectors/detector-cooling>.
- [13] F. Gagliardi, A. Ciotoli, and L. Lepore. «Novel Applications of State-of-the-Art Gamma-Ray Imaging Technique: From Nuclear Decommissioning and Radioprotection to Radiological Characterization and Safeguards». In: *EPJ Web of Conferences*. Vol. 288. 2023, pp. 7–13. DOI: 10.1051/epjconf/202328807013.
- [14] PHDS Co. *GeGI: Germanium Gamma-Ray Imaging HPGe Spectrometer*. Accessed: 2025-02-14. URL: <https://phdsco.com/wp-content/uploads/2024/05/20240514-GeGI-Front-and-Back-MK-DIGITAL-BEST.pdf>.
- [15] Jason M. Jaworski. «Compton Imaging Algorithms for Position-Sensitive Gamma-Ray Detectors in the Presence of Motion». PhD thesis. University of Michigan, 2013.
- [16] Z. He, W. Li, G. Knoll, D. Wehe, J. Berry, and C. Stahle. «3-D position sensitive CdZnTe gamma-ray spectrometers». In: *Nuclear Instruments and Methods in Physics Research Section A* 422 (1999), pp. 173–178. DOI: 10.1016/S0168-9002(98)00926-3.
- [17] F. Zhang, Z. He, D. Xu, G. Knoll, D. Wehe, and J. Berry. «Improved resolution for 3-D position sensitive CdZnTe spectrometers». In: *IEEE Transactions on Nuclear Science* 51 (2004), pp. 2427–2431. DOI: 10.1109/TNS.2004.836062.
- [18] H3D Inc. *Gamma-ray Imaging: Compton and Coded Aperture Imaging*. Accessed: January 13, 2025. URL: <https://h3dgamma.com/imaging.php>.
- [19] Filippo Gagliardi. «Integration of independent NDA techniques within a SLAM-based robotic system for improving safeguards standard routines: a review of the current status and possible future developments». In: *ESARDA Bulletin - The International Journal of Nuclear Safeguards and Non-Proliferation* 64.2 (2022), pp. 10–21. DOI: 10.3011/ESARDA.IJNSNP.2022.9.
- [20] *GammAware User Manual*. H3D Inc. 2021.
- [21] Filippo Gagliardi. «Enhancing Radiological Characterization Through Static 2D and Free-Moving 3D Gamma-Ray Imaging». PhD thesis. Sapienza Università di Roma, 2025.
- [22] *Visualizer 3D User Manual V3.0.8*. H3D, Inc. 2024.
- [23] S. Kaye, W. Kaye, J. Jaworski, and Z. He. «Experimental limitations of coded aperture imaging using thick 3D-position-sensitive CdZnTe detectors». In: *IEEE Nuclear Science Symposium & Medical Imaging Conference*. 2010, pp. 3856–3859. DOI: 10.1109/NSSMIC.2010.5874535.

BIBLIOGRAPHY

- [24] Nucleco. *Nucleco Company Profile*. Accessed: 2025-02-04. URL: <https://www.nucleco.it/RaccoltaDocumenti/2024/chi-siamo/Nucleco-Company-Profile-EN.pdf>.
- [25] Susan K. Smith and Dave Petroka. *TGS Technical Description For Automated TGS System*. Mirion Technologies (Canberra) GmbH. 2011.
- [26] Robert J. Estep and Stephen Croft. *TGS FIT Algorithms*. PowerPoint presentation. May 2006.
- [27] R.J. Estep, Los Alamos National Laboratory, United States. Department of Energy. Office of Safeguards, and Security. *TGS FIT: Image Reconstruction Software for Quantitative, Low-resolution Tomographic Assays*. Los Alamos National Laboratory, 1993.
- [28] Valles Parquet. *Compensato Pioppo - Compensato Multistrato*. Accessed: 2025-01-27. URL: <https://www.valles-parquet.it/compensato-multistrato/compensato-pioppo/>.
- [29] Hase Petroleum Wax Co. *Paraffin Wax*. Accessed: 2025-01-28. URL: https://www.hp wax.com/paraffin_wax.htm.
- [30] Oak Ridge Associated Universities. *Marinelli Beaker*. Accessed: 2024-11-01. ORAU Health Physics Historical Instrumentation Museum Collection. URL: <https://www.ornl.gov/health-physics-museum/collection/miscellaneous/beakers.html>.
- [31] GA-MA & Associates Inc. *Specialty Products for the Radiochemistry Laboratory: Marinelli Beakers Catalog*. May 2019.
- [32] GSM Arena. *Samsung Galaxy S20 Plus Specifications*. Accessed: 2025-01-23. URL: https://www.gsmarena.com/samsung_galaxy_s20+-10080.php.
- [33] Polycam. *Photogrammetry creator and viewer*. Accessed: 2025-01-23. URL: <https://poly.cam/tools/photogrammetry>.
- [34] Anette Eltner and Giulia Sofia. «Chapter 1 - Structure from motion photogrammetric technique». In: *Remote Sensing of Geomorphology*. Elsevier, 2020. DOI: <https://doi.org/10.1016/B978-0-444-64177-9.00001-1>.
- [35] Harvard Natural Sciences Lecture Demonstrations. *Alpha, Beta, Gamma Penetration and Shielding*. Accessed: 2025-01-23. URL: <https://sciencedemonstrations.fas.harvard.edu/presentations/%CE%B1-%CE%B2-%CE%B3-penetration-and-shielding>.
- [36] CloudCompare Development Team. *Introduction to CloudCompare*. Accessed: 2025-01-29. URL: <https://www.cloudcompare.org/doc/wiki/index.php/Introduction>.

- [37] CloudCompare Forum. *Structured vs. Unstructured File Formats*. Accessed: 2025-01-30. URL: <https://www.cloudcompare.org/forum/viewtopic.php?t=3294>.
- [38] Cintoo US Inc. *Structured vs. Unified & Unstructured Scan Data*. Accessed: 2024-01-30. URL: <https://help.cintoo.com/support/solutions/articles/101000461922-structured-vs-unified-unstructured-scan-data>.
- [39] Szymon Rusinkiewicz and Marc Levoy. «Efficient variants of the ICP algorithm». In: *Proceedings Third International Conference on 3-D Digital Imaging and Modeling*. 2001, pp. 145–152. DOI: 10.1109/IM.2001.924423.
- [40] Point Cloud Library (PCL). *Statistical Outlier Removal Filter Tutorial*. Accessed: 2025-01-30. URL: https://pcl.readthedocs.io/projects/tutorials/en/master/statistical_outlier.html.
- [41] Richard Szeliski. «Feature-based alignment». In: *Computer Vision: Algorithms and Applications*. Springer London, 2011, pp. 273–301. DOI: 10.1007/978-1-84882-935-0_6.
- [42] CloudCompare. *Mesh: Delaunay 2.5D (XY plane)*. Accessed: 2025-02-14. URL: [https://www.cloudcompare.org/doc/wiki/index.php/Mesh%5C%5CDelaunay_2.5D_\(XY_plane\)](https://www.cloudcompare.org/doc/wiki/index.php/Mesh%5C%5CDelaunay_2.5D_(XY_plane)).